JGR Planets

RESEARCH ARTICLE
10.1029/2021JE007025

Key Points:

- Ocean circulation on icy moons induced by heating from below is explored by numerical simulation
- Non-dimensional numbers characterize the influence of the moon's rotation and geometry of the tangent cylinder
- Scaling laws backed by our experiments are extended to parameters typical of real icy moons allowing us to speculate on their circulation

Correspondence to:
S. Bire,
bire@mit.edu

Citation:
Bire, S., Kang, W., Ramadhan, A., Campin, J.-M., & Marshall, J. (2022). Exploring ocean circulation on icy moons heated from below. *Journal of Geophysical Research: Planets*, *127*, e2021JE007025. https://doi.org/10.1029/2021JE007025

Received 25 AUG 2021
Accepted 28 FEB 2022

Exploring Ocean Circulation on Icy Moons Heated From Below

Suyash Bire[1], Wanying Kang[1], Ali Ramadhan[1], Jean-Michel Campin[1], and John Marshall[1]

[1]Department of Earth, Atmospheric, and Planetary Sciences, Massachusetts Institute of Technology, Cambridge, MA, USA

Abstract We numerically explore convection and general circulation of an ocean, encased in a spherical shell of uniform thickness, heated from below by a spatially uniform heat flux, and whose temperature at the upper surface is relaxed to the freezing point of water. The role of salt is not considered. We describe the phenomenology and equilibrium solutions across a broad range of two key non-dimensional numbers: the natural Rossby number, a measure of the influence of rotation, and the ratio of inner to outer radius of the moon's ocean, a measure of the geometry of the moon's tangent cylinder. Two distinct regimes of circulation are identified, both dominated by Taylor columns aligned with the rotation axis—"plumes" and "rolls" which predominate inside and outside the tangent cylinder, respectively. Inside the tangent cylinder, convective plumes align with Taylor columns that extend from the bottom to the ice shell. The plumes energize geostrophic turbulence which in turn generates a general circulation consisting counter-rotating zonal jets. Moreover, the plumes are efficient at transferring heat from the bottom to the surface, resulting in loss of heat from the ocean to the polar ice. If the plumes are suppressed rolls outside the tangent cylinder become the dominant mode of heat transfer resulting in equatorial cooling. We conclude that if moons such as Enceladus and Europa were to be predominantly heated from below, they will likely have a "Jovian-like" circulation: an unstratified, turbulent, geostrophically controlled ocean with strong "Taylor column" behavior and a circulation dominated by counter-rotating zonal jets.

Plain Language Summary Subsurface oceans on the icy moons of our Solar System are receiving increasing attention in the search for extraterrestrial life. It is thus important to understand the dynamics of these oceans and identify circulation pathways and timescales. Here, we use numerical simulations to explore likely ocean circulations if the primary energy source is geothermal heating from below. We describe the phenomenology of the resulting circulation patterns as the assumed rotation rate and ocean depth is varied. Key non-dimensional numbers are identified, and used to organize our study, informing speculations about the nature of the circulation of real icy moons. Based on best estimates of controlling non-dimensional parameters, we argue that the ocean circulations on Europa and Enceladus are likely to be very strongly influenced by rotation and manifest multiple alternating bands of zonal currents flowing in opposite direction, with distinctly different tropical and extratropical regimes. The likely nature of the small-scale turbulence and convection excited by bottom heating, which energizes the zonal jets, is also described.

1. Introduction

Icy moons with subsurface oceans, such as Enceladus (Thomas et al., 2016) and Europa (Hand & Chyba, 2007), are targets in the search for extraterrestrial life. Not only is there a liquid water ocean on these icy moons, but also the ocean appears to be salty (Postberg et al., 2009; Trumbo et al., 2019), indicating present or past interactions between the ocean and the silicate core beneath. Methane and macromolecular organic compounds have been detected in the sprays emanated from the geysers on the south pole of Enceladus (Postberg et al., 2018; Waite et al., 2006). Tholin, an abiotic organic compound that may facilitate prebiotic chemistry formation (Borucki et al., 2002) and provide food for heterotrophic microorganisms before autotrophy evolved (Stoker et al., 1990), has been found on the surface of Europa (Borucki et al., 2002). Such evidence suggests a very high astrobiological potential of icy moon worlds. However, our understanding of the physical and chemical processes going on in the ocean, ice shell, and silicate core are still very limited. Among all the puzzles that face us, ocean dynamics is of particular importance because it results in transport of heat, salt, and potential biosignatures between the core up to the ice shell.

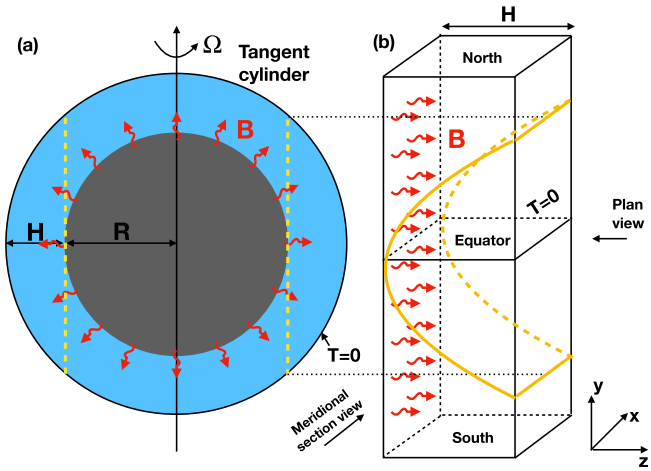

Figure 1. (a) Geometry of the ocean of an idealized icy moon. The gray region represents the silicate core of radius R which is enveloped by a liquid ocean of depth H shown in blue. The ice shell is the white exterior region and not marked. The red arrows pointing radially outwards represent the imposed buoyancy flux B due to heating at the ocean bottom. The temperature at the upper boundary is relaxed to 0°C. At equilibrium the heat flux emanating from the bottom is lost through the upper surface. The axis of rotation of the whole system is along Ω. The two dotted yellow lines mark the tangent cylinder. The ratio $\eta = R_i/R_o$, where $R_i = R$ and $R_o = R + H$ are the inner and outer radii, respectively. (b) The Cartesian geometry assumed by our deep beta-plane model extending from pole to pole across the equator. The poles are replaced by walls and the east-west flow is periodic. Note that the tangent cylinder of the spherical shell becomes a parabola-like surface in the Cartesian model, as indicated. The temperature at the surface is relaxed to 0°C. A uniform buoyancy flux B is imposed at the bottom as shown. We assume a linear equation of state in which the density only depends on the temperature. This assumption, together with a specification of a (constant) gravitational acceleration, defines Ro^*.

The four major drivers of ocean circulation on icy moons are bottom heating (Amit et al., 2020; Soderlund, 2019; Soderlund et al., 2013), the salinity flux induced by freezing and melting of ice (Ashkenazy & Tziperman, 2021; Lobo et al., 2021), the temperature variation just beneath the ice-shell due to the dependence of the freezing point of water on pressure (Kang et al., 2021), and tidal heating (Matsuyama et al., 2018; Tyler, 2014). In this work, we focus on the first and do not address the others. Our goal is to explore how ocean dynamics depend on the depth, the heat flux prescribed at the bottom and the rotation rate of the moon, as illustrated schematically in Figure 1. We do this by identifying key non-dimensional numbers that govern the dynamics. A further goal will be to explore how ocean dynamics carry heat coming in at the bottom up to the ice shell above, the resulting temperature distribution within the ocean, and the general circulation that is set up.

Inspired by the circulation in Earth's core and in the atmospheres of Jovian planets, there is a vast body of literature on rotating convection in fluid contained within spherical shells that is directly applicable to the problem of circulation on icy moons heated from below. A key result of these studies is that the dynamics behave differently inside and outside the tangent cylinder—a cylinder whose sides are parallel to the moon's axis of rotation and are tangential (hence the name) to the ocean's floor at the equator (Figure 1). Roberts (1968) and F. H. Busse (1970) were among the first to study the problem of convection in rotating spherical shells and found that the convection outside the tangent cylinder is organized to form “rolls,” Taylor columns aligned along the axis of rotation but perpendicular to gravity. Inside the tangent cylinder one observes “plumes,” convection in the direction of gravity where now the gravity and rotation vectors are more aligned. Laboratory studies by Cardin and Olson (1992), Aubert et al. (2001), and Aurnou et al. (2003) provide further confirmation of the nature of convection in spherical shells. Dormy et al. (2004) and Takehiro (2008) derive analytical solutions for the emergence of rolls in rotating spherical shells. More recently, Gastine et al. (2016) have proposed a regime diagram characterizing convection in a spherical shell.

Rhines (1975) introduced a spatial scale, now known as the “Rhines scale,” at which the inverse cascade in geostrophic turbulence energized, for example, by convection, is arrested through the excitement of Rossby waves, resulting in zonal jets. This scale has been invoked to explain the nature of jets on Jovian atmospheres by, for example, Williams (1979) and more recently Dowling (1995); Kaspi and Flierl (2007); and Heimpel and Aurnou (2007) among others.

Applying insights from these studies to the oceans on icy moons, Vance and Goodman (2009) speculate that they are likely to be very weakly stratified and have counter-rotating zonal jets in geostrophic balance. Soderlund et al. (2013), instead, suggest that the circulation on Europa might be under weak rotational control and dominated by an eastward jet at the equator and flanked by broad westward flow poleward of it. Further studies by Soderlund (2019) and Amit et al. (2020) suggest that the pattern of heat loss from the ocean to the ice on Europa could depend upon the nature of convection in the ocean and how it is influenced by rotational and diffusive/viscous effects. Recently, in a study of Europa, Ashkenazy and Tziperman (2021) account for the effect of salinity due to the freezing/melting of a flat ice sheet and find that the vertical heat flux tends to be slightly focused toward the pole. The dynamics in their solution is strongly constrained by rotation.

The modus operandi of many such studies, and certainly our study here, is to identify key controlling non-dimensional parameters, perform experiments in parameter space that can be reached numerically, and then extrapolate from them to the regimes where icy moons are thought to occupy. In almost all such previous studies the non-dimensional numbers employed are typically the Rayleigh number (Ra) and Ekman number (E), both of which depend on the eddy viscosity and diffusivity assumed in the model, and the temperature difference imposed across the water column. Appropriate values of Ra and E for icy moons are not known with any certainty because

turbulent processes must be represented by eddy viscosities and diffusivities which are not distinct from the convective process itself.

Here, as discussed in detail below, we choose to characterize the fluid dynamics in terms of the natural Rossby number, Ro^*—(Jones & Marshall, 1993; Marshall & Schott, 1999; Maxworthy & Narimousa, 1994)—defined by:

$$Ro^* = \left(\frac{B}{f^3 H^2} \right)^{1/2}. \quad (1)$$

Ro^* depends only on parameters external to the fluid: the buoyancy flux, B, being carried across the fluid (defined in Section 3 below), the rotation rate, $f = 2\,\Omega$, and the depth of the fluid, H. It can be interpreted as the ratio of the timescale it takes for a fluid parcel to rise a depth H in convection driven from below with a buoyancy flux B, to the timescale set by rotation f. Its use leads to a tidy division of the controlling parameters between a rotational parameter independent of diffusion (Ro^*) and a viscous/diffusive parameter (E). This is especially useful for application to icy moons because, although Ro^* is somewhat constrained by observations, the Ra number is rather uncertain because, as noted above, it depends on poorly known values of eddy diffusivity and viscosity.

We find that Ro^* has great utility in organizing our experiments and putting them in the context of likely flow regimes on icy moons. Moreover, we show that the intensity and spatial scale of turbulent motions and their efficiency of radial heat transport can be rationalized in terms of Ro^* across a vast range of Ro^* values, from very small (the icy moon regime) to large (more typical of convection on Earth's atmosphere).

Another non-dimensional parameter we employ is a measure of the geometry of the moon and in particular its tangent cylinder, $\eta = R_i/(R_i + H)$ where R_i and H are the inner radius and depth of the moon's ocean, respectively. When η is close to unity the fluid shell is thin; as it decreases the fluid deepens and the influence of Taylor-Proudman (Pedlosky, 1987) and the tangent cylinder is felt over a larger meridional fraction of the spherical domain. When Ro^* is small and the ocean is deep, two distinct regions emerge demarcated by the tangent cylinder—upright, plumy convection occurs at higher latitudes inside the tangent cylinder, whereas roll-like "Busse" convection (F. H. Busse, 1970) occurs in tropical latitudes outside of it.

Our paper is set out as follows. Section 2 sets up the problem and identifies key non-dimensional numbers: the (Ro^*, E) pairing and the geometrical factor η. We have a particular interest in where Europa and Enceladus lie in this phase space. Section 3 describes the numerical strategy and boundary conditions employed. Rather than prescribe a temperature difference across the fluid we impose a heat flux at the lower boundary and relax the fluid to the freezing point of water at the upper boundary. Section 4 describes and interprets the solutions obtained as key non-dimensional numbers are changed. Finally, in Section 5, we summarize and conclude.

2. Convection in a Rotating Spherical Shell Driven by Heating From Below

What is the nature of the convective activity driven by heating from below in a deep spherical shell that comprises an icy moon? Under what circumstances is the convection rotationally controlled so that Taylor-Proudman constraints dominate? What are the implications of those rotational constraints on the general circulation of an ocean in a deep spherical shell? As sketched in Figure 1 the external parameters of our problem are the inner radius of the moon R_i, the depth of the ocean H, the rotation rate of the moon Ω, and the buoyancy flux B emanating from the silicate core. These are all somewhat constrained by observations thus enabling us to place, for example, Enceladus and Europa in (Ro^*, η) phase space.

2.1. Scaling Ideas

For clarity, we begin by briefly reviewing key scaling ideas which will be used to frame our study. These are motivated by the literature on open ocean convection reviewed by Marshall and Schott (1999). Given that the timescale for fluid rising in a convective element from below on a small but deep icy moon, gently heated from below, is likely to be very many rotation periods, we expect Ro^* to be small. Thus, the dynamics can be expected to be profoundly influenced by the rotation of the moon, as will be clear from the numerical experiments presented herein. To demonstrate the nature of rotational constraints in a deep fluid we will also explore how the nature

of the solution changes as the Rossby number is increased and the fluid depth decreases. In an Appendix A, we connect our study to the wider rotating convection literature, placing our study in the context of previous work and, in particular, (Ra, E) space.

2.1.1. Influence of Rotation

Imagine that warming from below associated with a sustained buoyancy flux of magnitude B drives convection into water of depth H as illustrated schematically in Figure 1. A layer of 3-D, buoyancy-driven turbulence will deepen as the plumes that make it up evolve in time, penetrating into the fluid above. Ultimately, the convection will extend over the entire depth H. We now briefly review the scales which naturally emerge.

2.1.1.1. Evolution Over Time

Let us suppose that in the initial stages, plumes extending into the convective layer are so small in scale that they cannot feel the finite depth H. Furthermore for times $t \ll f^{-1}$ (where $f = 2\ \Omega$), rotation is unimportant; only B remains as the controlling parameter. It is then not possible to construct scales for the depth, buoyancy, or velocity of the plumes. The convective process must evolve in time, and we suppose that it proceeds in a self-similar way. The following scales can be formed from B (units of velocity times acceleration) and t (a more detailed account can be found in Jones and Marshall (1993) and Maxworthy and Narimousa (1994)):

$$l \sim \left(Bt^3\right)^{1/2}; u \sim (Bt)^{1/2}; g' \sim \left(\frac{B}{t}\right)^{1/2} \tag{2}$$

where l is a measure of the length scale of the convective motion, u is a velocity scale, and g' is a measure of the reduced gravity, defined by

$$g' = g\frac{\delta\rho}{\rho_{\text{ref}}}, \tag{3}$$

where $\delta\rho$ is the density anomaly of a fluid parcel relative to its surroundings and ρ_{ref} is a constant reference density. Note that the buoyancy of a fluid parcel is just the negative of the reduced gravity $b = -g'$.

2.1.1.2. Scale Constrained by Ocean Depth

If it is the depth H that ultimately limits the scale of the cells then putting $l = H$ in Equation 2, above, the following scaling is suggested (Deardorff, 1980), independent of rotation:

$$l \sim l_{\text{norot}} = H; u \sim u_{\text{norot}} = (BH)^{1/3}; g' \sim g'_{\text{norot}} = \left(\frac{B^2}{H}\right)^{1/3} \tag{4}$$

The subscript "norot" indicates that these are the scales adopted in the absence of rotation.

2.1.1.3. Scale Constrained by Rotation

If H is sufficiently large then the evolving convection will come under rotational control before it reaches the surface. The transition from 3-D buoyancy-driven plumes to quasi-2-D, rotationally dominated motions, will occur as t approaches f^{-1}, at which point, replacing t by f^{-1} in Equation 2, the following scales pertain (Fernando et al., 1991):

$$l \sim l_{\text{rot}} = \left(\frac{B}{f^3}\right)^{1/2}; u \sim u_{\text{rot}} = \left(\frac{B}{f}\right)^{1/2}; g' \sim g'_{\text{rot}} = (Bf)^{1/2} \tag{5}$$

where the subscript "rot" (for "rotation") has been used to denote the scales at which rotation begins to be important. As the plumes keep supplying warm water upwards, they eventually coalesce to form a columnar structure stretching from the bottom all the way to the top (Jones & Marshall, 1993). If the column has a buoyancy anomaly set by the entraining, rotationally constrained plumes given by g'_{rot}, then there is a scale given by

$$l_\rho = \frac{\sqrt{g'_{\rm rot} H}}{f} = (l_{\rm rot} H)^{1/2}, \tag{6}$$

which is called the Rossby radius of deformation. The numerator, $\sqrt{g'_{\rm rot} H}$, is the speed of the gravity waves set off by the buoyancy forcing. Thus, l_ρ is a measure of the distance gravity waves travel before being influenced by rotation. Here, the constraining nature of rotation manifests as the aggregation of small plumes into rolls that scale as l_ρ, as discussed in more detail in Section 4.1.

It should be noted that the foregoing scales are independent of assumptions concerning eddy viscosity and diffusivity provided that they are sufficiently small; they are the velocity, space, and buoyancy scales that can be constructed from the "external" parameters B, f, and H. However, the constants of proportionality in Equations 4 and 5 will be dependent on viscous/diffusive processes and can be determined experimentally from laboratory and numerical experiments. Below, we will present numerical experiments which test and provide broad support for these scaling ideas in the context of icy moons.

2.2. Key Non-Dimensional Numbers

It is important to identify key non-dimensional numbers that govern the problem because more often than not, it is not possible to carry out numerical experiments in realistic parameter regimes. However, by extrapolation, we can infer likely behavior of the real system if parameters are appropriately set. Here, we focus on key parameters that characterize the influence of rotation on the convective motion, and the geometry of the spherical shell in which it is occurring.

2.2.1. The Natural Rossby Number

The natural Rossby number, Equation 1, can be written as the ratio of $l_{\rm rot}$, the scale at which convection comes under the influence of rotation, to the total depth of the fluid H thus:

$$Ro^* = \frac{l_{rot}}{H}, \tag{7}$$

providing another physical interpretation of it. The scaling for rotating and non-rotating convection presented above can now be written out entirely in terms of Ro^* thus:

$$\frac{u_{\rm norot}}{f H} = Ro^{*\,2/3} \tag{8}$$

$$\frac{g'_{\rm norot}}{f^2 H} = Ro^{*\,4/3}, \tag{9}$$

and

$$\frac{u_{\rm rot}}{f H} = Ro^*, \tag{10}$$

$$\frac{g'_{\rm rot}}{f^2 H} = Ro^* \tag{11}$$

The deformation scale in Equation 6 can be written:

$$\frac{l_\rho}{H} = \sqrt{Ro^*}. \tag{12}$$

We will test these scaling laws in our simulations of icy moons presented in Section 4 below.

2.2.2. Deep Oceans and the Geometry of the Tangent Cylinder: Aspect Ratio $\eta = R_i/(R_i + H)$

The scaling ideas reviewed above are applied here to convection in a rotating spherical shell. When $Ro^* \ll 1$, Taylor columns align parallel to the rotation axis. In this limit, the convective dynamics behave differently inside and outside the tangent cylinder. Upright convection takes place inside the tangent cylinder, whereas roll-like

Table 1
Typical Physical Parameters and Key Non-Dimensional Numbers for Icy Moons Inspired by Soderlund (2019), Compared to Those That Characterize Typical Atmospheric and Oceanic Convection on Earth (Marshall & Schott, 1999)

	Enceladus	Titan	Europa	Ganymede	Earth atmos.	Earth ocean
g (ms^{-1})	0.1	1.4	1.3	1.4	9.81	9.81
Ω (10^{-6} s^{-1})	53	4.6	21	10	73	73
Q ($mW\,m^{-2}$)	80	20	100	40	2×10^5	2×10^5
P (10^3 $kg\,m^{-3}$)	1	1.2	1.1	1.2	10^{-3}	1
C_p ($10^3 J\,kg^{-1}\,K^{-1}$)	4	3	3.8	3	4	4
α ($10^{-4} K^{-1}$)	0.1	3	2	2.5	30	2
B (10^{-12} $m^2 s^{-3}$)	0.02	2.3	6.4	3.9	6×10^9	1×10^5
H (km)	40	300	120	300	10	4
R_o (km)	252	2,575	1,561	2,631	6,400	6,400
H	0.84	0.88	0.92	0.89	0.9984	0.9993
Ro^* ($\times 10^{-6}$)	3.2	180	77	73	4.4×10^6	4.5×10^4

Note. Many of the quantities in the first four columns are rather uncertain due to incomplete knowledge of the depth and composition of the ocean on icy moons. See Table 4 for the possible range of various parameters on Europa and Enceladus.

convection takes place outside it (e.g., Gastine et al., 2016). The distinction between the two can be understood by the alignment of the axis of rotation with gravity. In purely upright convection the axis of rotation and gravity are aligned, while in roll-like convection the axis of rotation is perpendicular to gravity. The latitude at which the tangent cylinder intersects the surface depends on the depth of the ocean. The ratio of inner and outer radii, $\eta = R_i/(R_i + H)$, therefore, is the other key non-dimensional number that determines the dynamics and heat transport properties, in addition to Ro^* (e.g., Al-Shamali et al., 2004).

2.2.3. Typical Non-Dimensional Numbers for Icy Moons

Without running any experiments, the two aforementioned non-dimensional numbers, Ro^* and η, can inform us about the likely dynamics on icy moons. Key physical parameters and derived non-dimensional numbers for four major icy satellites, Enceladus, Titan, Europa, and Ganymede, are summarized in Table 1 and compared to typical terrestrial atmospheric and oceanic values. The natural Rossby number Ro^* for all these icy satellites is smaller than 2×10^{-4}, indicating that tens of thousands of rotation periods would have passed before a buoyant water parcel rising from the bottom makes it to the surface. Thus, we expect ocean dynamics to be strongly constrained by rotation. This should be contrasted with Earth's atmosphere in which $Ro^* \sim 1$ and Earth's ocean where $Ro^* \sim 0.01$. Note that these values can be elevated to as high as 10 and 0.1 for atmosphere and ocean, respectively, in regions of intense localized convection like the Mediterranean Ocean (Marshall & Schott, 1999). However, on a global scale, the ocean on these icy satellites has more in common with Earth's ocean, hence the purported relevance of the scaling ideas developed for open ocean deep convection presented in Section 2.1. The ratios of inner to outer radii η on icy moons are around 0.8–0.9, so the fluids are deep. This is in contrast to the shallow atmosphere and ocean on Earth where η is all but unity. Thus, we will have to relax the shallow fluid approximation and include all components of the Coriolis force. In the remainder of our paper, we will perform an array of ultra-high resolution numerical experiments to explore the two dimensional parameter space of Ro^* and η to fill in the detailed dynamics.

3. Modeling Framework

We adopt a highly idealized equation of state in which the buoyancy depends only on temperature assuming a thermal expansion coefficient, α, which is constant and positive, appropriate if the ocean is sufficiently salty. The buoyancy, $b = -g\,\delta\rho/\rho_{ref}$, where $\delta\rho$ is the density anomaly (see Equation 3) is related to temperature, T, by a linear equation of state,

$$b = \alpha g\,(T - T_{ref})\,, \tag{13}$$

and T_{ref} is a reference temperature.

At the upper boundary we relax the temperature to the freezing point of water set here to a constant value of 0°C. The circulation is energized by imposing a spatially uniform heat flux at the bottom of the ocean, Q, implying a buoyancy flux, B, given by

$$B = \frac{\alpha g Q}{\rho_{ref} C_p}, \tag{14}$$

where C_p is the specific heat capacity of water. This should be contrasted with the classic (Rayleigh) convection problem in which a temperature contrast is imposed across the fluid. Although unlikely to introduce significant changes (Aurnou et al., 2020; Calkins et al., 2015; Johnston & Doering, 2009), it is satisfying to note that here the bulk vertical temperature gradient is not externally set but becomes part of the solution. Because the boundary conditions are homogeneous in space, any emergent structures and spatial scales must be a consequence of rotational, geometrical (spherical shell), and fluid-dynamical effects.

3.1. Deep β-Plane in Cartesian Coordinates Incorporating Non-Traditional Coriolis Terms

We use a Cartesian framework to represent fluid dynamics in spherical geometry that capture the change with latitude of the angle between the rotation vector and gravity. Derivations of such equation sets was pioneered by Grimshaw (1975), who wrote down a non-traditional β-plane set for a fluid on a rotating planet in which the vertical component of the Coriolis parameter was allowed to vary in the horizontal, whilst the horizontal component (set to zero on the traditional β-plane) was kept constant. Dellar (2011) significantly advanced Grimshaw's work by using Hamilton's principle to derive a non-traditional set in which both components of Coriolis are allowed to vary in latitude, without sacrificing conservation properties. We employ an equation set inspired by Dellar's work appropriate for a deep fluid in which the moon's rotation vector, Ω, and gravity, $\mathbf{g}$, are not parallel to one-another.

In Cartesian coordinates (x, y, z) with x, pointing eastwards, y pointing northwards and z pointing upwards in the direction opposite to gravity, the equations including a treatment of non-traditional Coriolis terms are written thus:

$$\frac{Du}{Dt} + \tilde{f} w - f v = -\frac{1}{\rho_{ref}} \frac{\partial p}{\partial x} + F^x, \tag{15}$$

$$\frac{Dv}{Dt} + f u = -\frac{1}{\rho_{ref}} \frac{\partial p}{\partial y} + F^y, \tag{16}$$

$$\frac{Dw}{Dt} - \tilde{f} u - b = -\frac{1}{\rho_{ref}} \frac{\partial p}{\partial z} + F^z, \tag{17}$$

where $\mathbf{u} = (u, v, w)$ is the velocity, b is the buoyancy, p is the pressure, $\frac{D}{Dt} = \frac{\partial}{\partial t} + \mathbf{u} \cdot \nabla$ is the total derivative, and the F's on the RHS represent momentum sources and sinks given by

$$(F^x, F^y, F^z) = \nu \nabla^2 \mathbf{u}, \tag{18}$$

where ν is the viscosity. Additionally, no-slip boundary conditions act as sinks of momentum at the bottom and on the sidewalls. We assume free-slip conditions at the top.

The Coriolis parameter is

$$\mathbf{f} = \left(0, \tilde{f}, f\right) = 2\Omega(0, \cos(y/R), \sin(y/R)), \tag{19}$$

where y/R increases from 0 to $\pi/2$ and R is the radius of the moon, allowing us to mimic the mis-alignment of the rotation vector and gravity on the sphere but in a Cartesian framework (see the Taylor Columns aligned with the rotation vector in Figure 2).

Along with the momentum equations we have the continuity equation,

$$\nabla \cdot \mathbf{u} = 0. \tag{20}$$

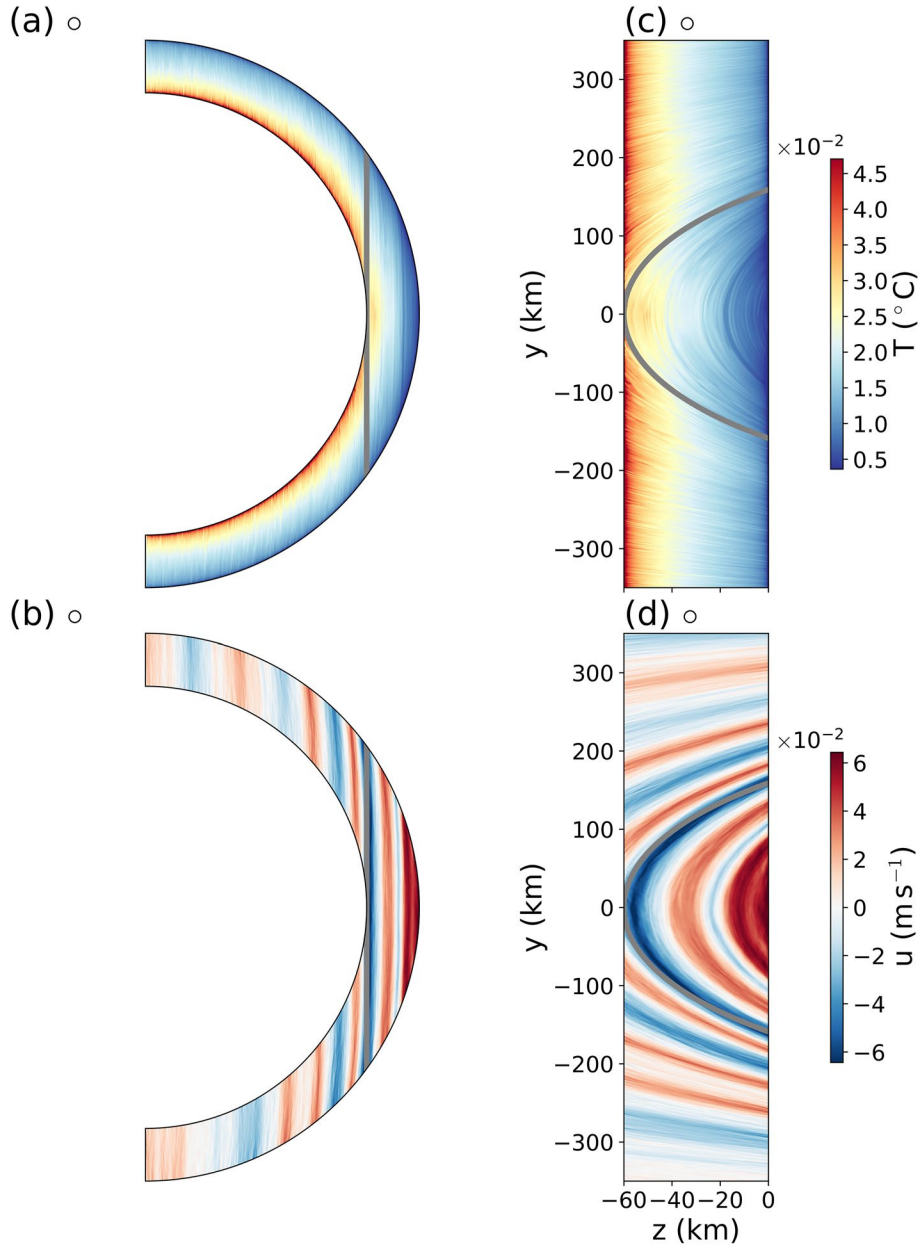

Figure 2. Sections of instantaneous (a) temperature and (b) zonal velocity from our reference experiment, row ∘ of Table 2, showing the alignment of convection with the local rotation vector in a deep spherical shell governed by deep beta-plane dynamics. The model extends from −90° to 90°N, and simulates a domain of width 50 km. Panels (c and d) show the same quantities as in panels (a and b), respectively, but in Cartesian coordinates used in the numerical simulations. The tangent cylinder, which appears to be curved in Cartesian coordinates, is shown by the thick gray lines, as set out schematically in Figure 1. Units are indicated by the color bar in °C for T and ms^{-1} for u.

Temperature evolves in time according to the equation

$$\frac{\mathrm{D}T}{\mathrm{D}t} = \kappa\nabla^2 T + \delta_{\mathrm{top}}\frac{T - T_0}{\tau} + \frac{\delta_{\mathrm{bottom}}}{\Delta z}\frac{Q}{\rho_{\mathrm{ref}} C_{\mathrm{p}}}, \tag{21}$$

where κ is the diffusivity, $\delta_{\mathrm{top}} = 1$ at the top and zero elsewhere, $\delta_{\mathrm{bottom}} = 1$ at the bottom and zero elsewhere, Δz is the vertical grid spacing and τ sets the relaxation timescale of temperature to the temperature prescribed at the upper boundary.

Table 2
A Summary of the Simulations Carried Out in Our Study, Along With Corresponding Key Dimensional and Non-Dimensional Numbers – See Also the Discussion in Appendix A and Table A1.

	H (km)	Q (W m^{-2})	Ω (10^{-5} s^{-1})	Ro^* ($\times 10^{-5}$)	η	l_ρ (km)	E ($\times 10^{-8}$)	Ra ($\times 10^{10}$)	Nu ($\times 10^{3}$)
⊞	10	500	5.3	410	0.96	0.65	180	1.2	0.23
⊕	10	50,000	5.3	4,100	0.96	2.06	180	6.3	4.4
⊗	10	100,000	0.53	1.9×10^5	0.96	13.75	1,800	4.4	13
+	30	500	5.3	140	0.88	1.12	21	36	0.58
†	30	50,000	5.3	1,400	0.88	3.53	21	190	11
×	30	100,000	0.53	6.2×10^4	0.88	23.58	210	140	30
∘	60	10	5.3	9.8	0.76	0.59	5.2	47	0.14
◁	60	500	5.3	69	0.76	1.58	5.2	260	1.3
▷	60	10,000	5.3	310	0.76	3.34	5.2	800	8.3
•	60	10	5.3	9.8	0.76	0.59	520	3.5×10^{-3}	1.9×10^{-3}
◀	60	500	5.3	69	0.76	1.58	520	1.9×10^{-2}	1.8×10^{-2}
▶	60	10,000	5.3	310	0.76	3.34	520	8.7×10^{-2}	7.6×10^{-2}

Note. Here, H is the height of the domain, Q is the prescribed bottom heat flux, Ω is the rotation rate of the moon, Ro^* is the natural Rossby number (Equation 1), η is the ratio of inner to outer radius, l_ρ is the deformation radius, Equation 12, E is the Ekman number (Equation A2), Ra is the Rayleigh number (Equation A1), and Nu is the Nusselt number (Equation A3).

3.2. Numerical Constants and Computational Details

Parameters for our reference experiment—row ∘ of Table 2—are inspired by what we know of Enceladus. We set the outer radius of the moon to $R_o = 251$ km and the rotation rate, Ω, to 5.30×10^{-5}s^{-1}. T_0 is set to 0°C and the relaxation timescale to it in Equation 21, $\tau = 2 \times 10^6$ s, or about 2.3 Earth days. Acceleration due to gravity $g = 0.1$ ms^{-2} and thermal expansion coefficient $\alpha = 1.67 \times 10^{-4}$°C^{-1}. Viscosity is set to 2×10^{-2}m^{2}s^{-1}, the smallest needed to maintain stability on the numerical grid, as described below. The Prandtl number (ratio of viscosity to diffusivity) for all experiments is set to unity. The heat flux, Q, is set to 10 W m^{-2}, in full knowledge of the fact that tidal heating rates on Enceladus imply fluxes which are orders of magnitude less, perhaps 80 mW m^{-2}. This is required to enable us to run multiple experiments out to steady state on a fine grid—see below. A key point, however, is that, as can be seen on row ∘ of Table 2, even with this large heat flux, our reference case has both $Ro^* \ll 1$ and η small, appropriate for Enceladus.

The above equations are discretized on a domain $x \subseteq [0, 50]$km, $y \subseteq [-395, 395]$km, and $z \subseteq [-H, 0]$, with $\Delta x = \Delta y = \Delta z = 300$ m and coded up in the framework provided by Oceananigans.jl (Ramadhan et al., 2020, 2021), open source software developed for studies of ocean processes. The eastern and western boundaries are periodic so our model is a re-entrant channel of width 50 km. The northern, southern, and bottom boundaries are walls with no slip boundary conditions, while the upper boundary has a free slip boundary condition. Oceananigans is written in the Julia programming language (Bezanson et al., 2017) and runs fast on GPUs enabled by Julia's native GPU compiler (Besard et al., 2019). To solve Equations 15–21 Oceananigans.jl uses a staggered C-grid finite volume spatial discretization (Arakawa & Lamb, 1977) with an upwind-biased 5th-order weighted essentially non-oscillatory advection scheme for momentum and tracers (Shu, 2009). Diffusion terms are computed using centered 2nd-order differences. A pressure projection method is used to ensure the incompressibility of **u**, Equation 20, at every time step (Brown et al., 2001). A fast Fourier-transform-based eigenfunction expansion of the discrete second-order Poisson operator is used to solve the discrete pressure Poisson equation for the pressure on a regular grid (Schumann & Sweet, 1988). An explicit 3rd-order Runge-Kutta method advances the solution in time (Le & Moin, 1991).

A snap-shot of the reference solution is shown in Figure 2. Since $Ro^* \ll 1$, we obtain a highly structured solution dominated by rotation in which the flow is aligned with the axis of the moon's rotation. We observe water at the bottom of the ocean warming up and rising in the water column, not in the direction of gravity, but rather in the direction of the rotation vector. Meanwhile zonal currents (both into and out of the page) comprise multiple

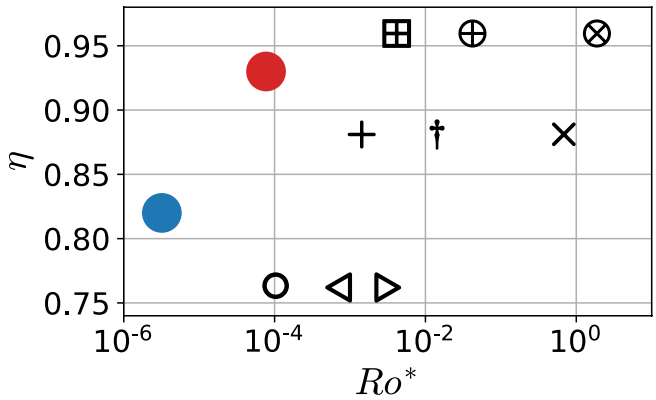

Figure 3. The position in (Ro^*, η) phase space of nine key experiments which span the phase space of the complete set of experiments set out in Table 2. The positions of Enceladus and Europa in this phase space are marked by blue and red circles, respectively.

counter-rotating zonal flows but which change little in the direction of Ω, a manifestation of the Taylor-Proudman theorem.

We carry out the suite of experiments summarized in Table 2, in which depths, heat fluxes, and rotation rates are varied. These are set out in graphical form as a function of Ro^* and η in our phase space plot, Figure 3. For reference, the position of Enceladus and Europa in this phase space is also marked. All experiments are integrated out to steady state. Note from Table 2 and Figure 3 we also carry out two experiments with a rotation rate which is 10 times slower than our reference, thus enabling us to explore much higher (Ro^*) regimes approaching that of convection in Earth's atmosphere and ocean. Additionally, three experiments with the smallest η are repeated but with a viscosity that is two orders of magnitude higher than in our reference experiment. They are not shown in Figure 3 because they occupy the same locations on our phase plot as the experiments with our reference viscosity.

4. Phenomenology of Ocean Circulations

We now present our solutions (Section 4.1), interpret them in terms of scaling laws for the intensity and scale of turbulent motions (Section 4.2), examine the nature of the counter-rotating zonal jets in terms of the "Rhines scale" and generalized thermal wind which connects them to meridional temperature gradients (Section 4.3), and discuss the parameters that control the latitudinal dependence of vertical heat transport at the upper boundary of the model (Section 4.4). In the first three parts, we will focus on the first nine experiments from Table 2 with our reference viscosity. The three experiments with higher viscosity are discussed in Section 4.4, where they help us explore solutions over a wider range of parameter space.

4.1. Convectively Driven Turbulence in the Spherical Shell

Figure 4 (plan view at mid-depth) and 5 (meridional section at $x = 25$ km) present instantaneous snapshots of the vertical velocity from nine solutions spanning (Ro^*, η) space chosen to highlight their nature and how they change with Ro^* and η. To help orientate the reader, meridional and plan views are illustrated schematically in Figure 1. All plots are shown after the solutions have reached statistical equilibrium. Black lines on the plan views mark where the tangent cylinder cuts through the mid-depth horizontal surface and, in the meridional sections, mark the positions of the tangent cylinder. On moving from left to right, Ro^* increases from small (order 10^{-4}) to large (order 1), and on moving in rows upwards, η increases from 0.76 to 0.96. In order that all quantities can be mapped using one scale, they are normalized w.r.t. their respective standard deviation, as set out in Table 3, and through use of which dimensional values can be inferred.

For small Ro^* it is clear that rotational constraints are very strong with the fluid being arranged in columns parallel to Ω. This is most clearly evident in our reference solution, in the bottom left of each figure, the one from which Figure 2 is taken. Outside the tangent cylinder (equatorward of the back lines) we see w organized into rolls, consistent with studies of convection in spherical shells (Aubert, 2005; Aurnou et al., 2003; Cardin & Olson, 1994; F. H. Busse, 1970; Gastine et al., 2016; Maas & Hansen, 2019; Miquel et al., 2018). Inside the tangent cylinder (poleward of the black lines) the convection is more granular and plumy (Aurnou et al., 2008; Gastine et al., 2016; Hindman et al., 2020). Recent observations from the Juno and Cassini missions to Jupiter and Saturn, respectively, suggest that the upper atmospheric circulations on these planets could be explained by this regime (Kaspi et al., 2018, 2020). For large Ro^* no such rotational constraint is felt and the convection is more sensitive to the direction of gravity than that of Ω.

In the fast rotating regime (marked by a small natural Rossby number), and in accord with the Taylor-Proudman theorem, flows tend not to vary along the axis of rotation, as is very clear from Figure 2. The influence of rotation is also evident in Figures 4g and 5g which show instantaneous w fields (in plan and meridional section), and in Figure 6g which shows instantaneous u (in meridional section) from the same solution. The differences in dynamics inside and outside the tangent cylinder arise from the differing orientation of the rotation axis with respect to that of gravity. Near the equator, the rotation axis, and therefore the direction of the Taylor columns, is almost

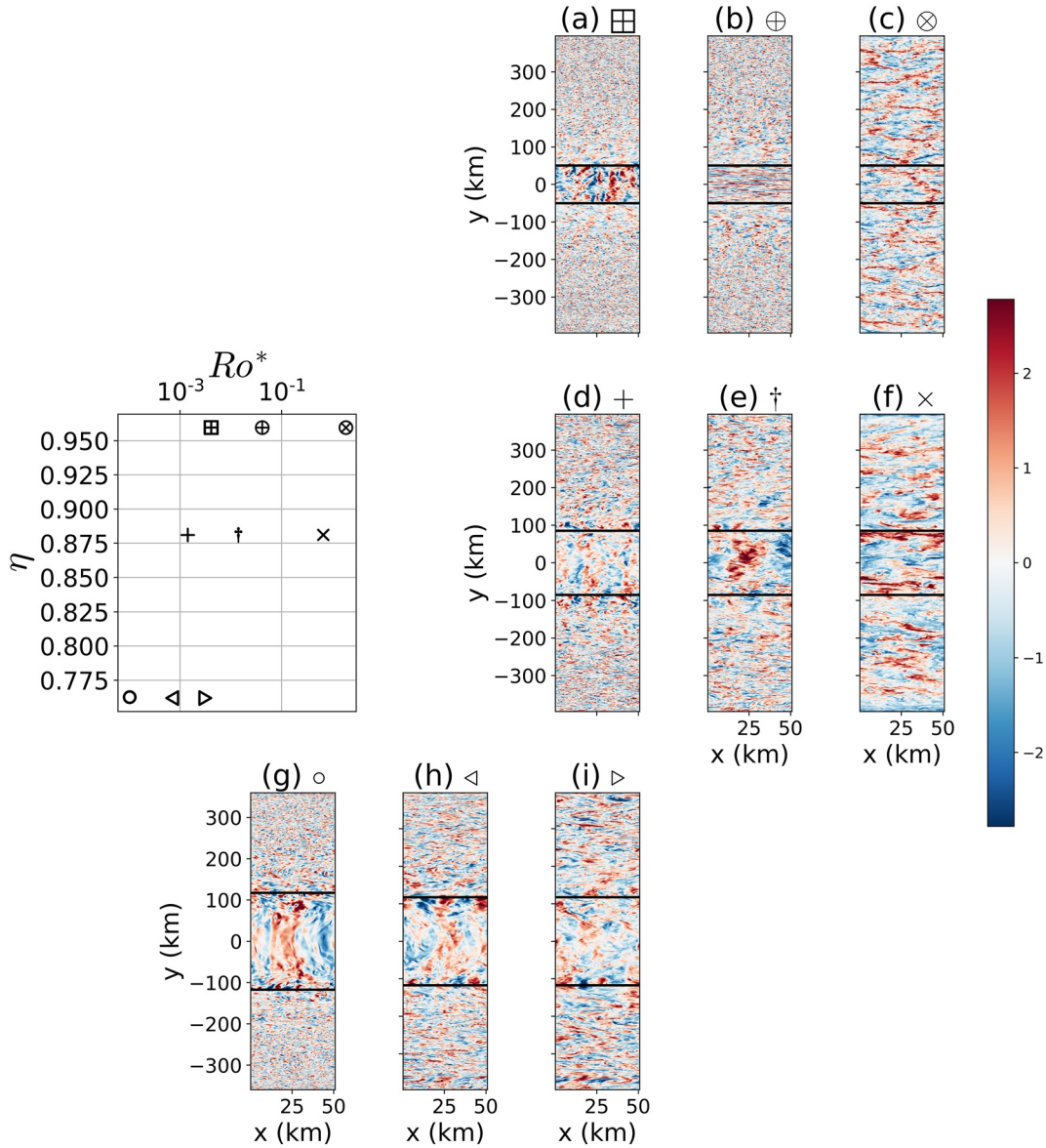

Figure 4. Plots of instantaneous vertical velocity anomalies normalized w.r.t. their standard deviation (see Table 3, $\left(w_{\mathrm{xy}} - \overline{w_{\mathrm{xy}}}\right) / \widehat{w_{\mathrm{xy}}}$ where xy indicates the horizontal plane) at mid-depth across our experiments. Here, the overbar represents a mean over the plane and the hat is the standard deviation relative to that mean. Note that the mean vertical velocity at any instant across any horizontal slice is zero, therefore, $\overline{w_{\mathrm{xy}}}$ is not shown in Table 3. The first, second, and third rows represent models with η of 0.96, 0.88, and 0.76, respectively. The natural Rossby number increases toward the right for each row. The latitude at which the tangent cylinder strikes the free surface is shown by the horizontal black line.

parallel to the lower boundary and thus perpendicular to gravity. Swirling motion in planes normal to Ω sweep fluid up and down in almost vertical planes. The rolls form through Rossby wave mode growth supported by the equivalent "β-effect" due to the gradual shortening of Taylor columns away from the rotating axis (Al-Shamali et al., 2004; Cardin & Olson, 1994; Dormy et al., 2004). With warm water rising and cold water sinking, these equatorial rolls transport heat upward, as shown in the equatorial cross section (Figure 7). In high latitudes, plumes predominate, shooting upward along the direction of the rotation axis while currents swirl around it. On reaching a statistically steady state, since tracers/heat are predominantly transported along the rotation axis, the heat flux reaching the upper surface is stronger over the poles than the equator—see Section 4.4 where this is discussed in much more detail.

Table 3
The Means $\overline{(\cdot)}$ and Standard Deviations $\widehat{(\cdot)}$ of Vertical Velocity (w), Zonal Velocity (u), and Temperature (T) Across Our Experiments

	$\widehat{w_{xy}}$ (mm s^{-1})	$\overline{w_{yz}}$ (mm s^{-1})	$\widehat{w_{yz}}$ (mm s^{-1})	$\overline{u}$(mm s^{-1})	$\hat{u}$(mm s^{-1})	$\overline{T}$(K)	$\hat{T}$(K)
⊞	14.5	−0.28	13.5	−3.86	90.7	1.16	0.07
⊕	71.7	1.92	64.6	−51.6	364	36.5	0.53
⊗	120	4.5	99.4	−42.4	195	50.9	0.45
+	15.8	0.675	14.3	12.5	137	0.56	0.06
†	90	4.65	83.8	−32.7	298	10.6	0.42
×	145	17.2	129	−723	467	25.1	0.54
∘	3.47	0.237	3.07	1.62	22.1	0.02	0.01
◁	18.5	3.37	16.5	3.2	123	0.23	0.05
▷	55.1	3.84	49.5	−5.92	258	1.32	0.20

Note. The subscripts $_{xy}$ and $_{yz}$ indicate the sections sampled: in an xy-plane at mid-depth and in a yz-plane at $x = 25$ km, respectively. All data is taken when solutions have reached a statistically steady state. Standard deviations tabulated here are used to non-dimensionalize our variables for plotting purposes.

This preference for heat transport by polar plumes can be clearly seen in the meridional plots of instantaneous temperature in Figures 8a, 8d and 8g-8i, in the low Ro^*, η experiments. Colder temperatures are typically found outside the tangent cylinder relative to inside, consistent with low heat transport toward the tropics from inside the tangent cylinder. An inhibition of meridional transport toward the tropics has been attributed to the presence of strong zonal flows along the tangent cylinder by Evonuk and Glatzmaier (2006), Aurnou et al. (2008), and Guervilly and Cardin (2017). Vance and Goodman (2009), on the other hand, presented a geometrical argument for a cold tropics. They argued that outside the tangent cylinder, Taylor columns never touch the bottom boundary and so, given the alignment of convection with them, the tropics should receive little heat from the bottom. In contrast, inside the tangent cylinder, Taylor columns reach from bottom to top providing a conduit for heat coming in at the bottom to reach the surface. Finally we note that panel f of Figure 8 is in a parameter regime similar to that of Soderlund et al. (2013) for Europa. In this solution most of the heat is being transported vertically in the tropics which are warmer than at high latitudes, and rotation has a much weaker effect on the circulation. Our calculations suggest, instead, that Enceladus and Europa might be more similar to the leftward solutions (more rotationally influenced) on our regime diagram.

In summary, when Ro^* and η are both small (lower left of Figures 4–6), one can vividly see the impact of the tangent cylinder on the motion, dividing the icy moon into two very different dynamical regimes. Low latitude regions outside the tangent cylinder are populated by meridionally aligned columnar rolls which extend out to the latitudes where the tangent cylinder strikes the surface. The smaller the value of η, the further away from the equator is this latitude (Figure 1), and greater is the fraction of the transport properties of the fluid being influenced by rolls.

As we move to the top right of Figures 4–6, the effect of rotation is much reduced, Ro^* is much larger, and the direction of g rather than Ω dominates, as seen in panel c (Gastine et al., 2016; Hindman et al., 2020). This diminishing of rotational influence from bottom left to top right panels will be evident in the scaling results we now discuss.

4.2. Intensity and Scales of Convective, Turbulent Motion

4.2.1. Temperature and Velocity Scales

We now infer the temperature, velocity, and length scales of the convective turbulence from our numerical simulations and compare them to the scaling laws outlined in Section 2.2.1. The temperature and velocity scales in the simulations are defined as:

$$T_{\text{conv}} = \sqrt{\overline{T'^2}}, \tag{22}$$

$$u_{\text{conv}} = \sqrt{\overline{u'^2} + \overline{v'^2}}, \tag{23}$$

where $u' = u - \bar{u}, v' = v - \bar{v}, T' = T - \bar{T}$ and $\overline{(\cdot)}$ denotes a horizontal and time average taken over the entire zonal width and 10 days, respectively. The black markers in Figures 9a–9c were obtained between $y = 10$ and 50 km typical of the equatorial region outside the tangent cylinder, while the red markers were obtained for $y = 200$ to 300 km indicative of the polar regions inside the tangent cylinder. A vertical average was also taken in order to collapse the data to a single point for each experiment.

In Figures 9a and 9b, the diagnosed horizontal and vertical velocity scales from Equation 23 are compared against predictions from our scaling, Equations 8 and 10. In panel c, the reduced gravity scales, given by $g'_{\text{conv}} = \alpha g T_{\text{conv}}$, are compared against our scaling prediction, Equations 9 and 11. To ease comparison, predicted slopes are indicated by the orange (non-rotating) and blue (rotating) straight lines. To a useful degree, we see that data from our

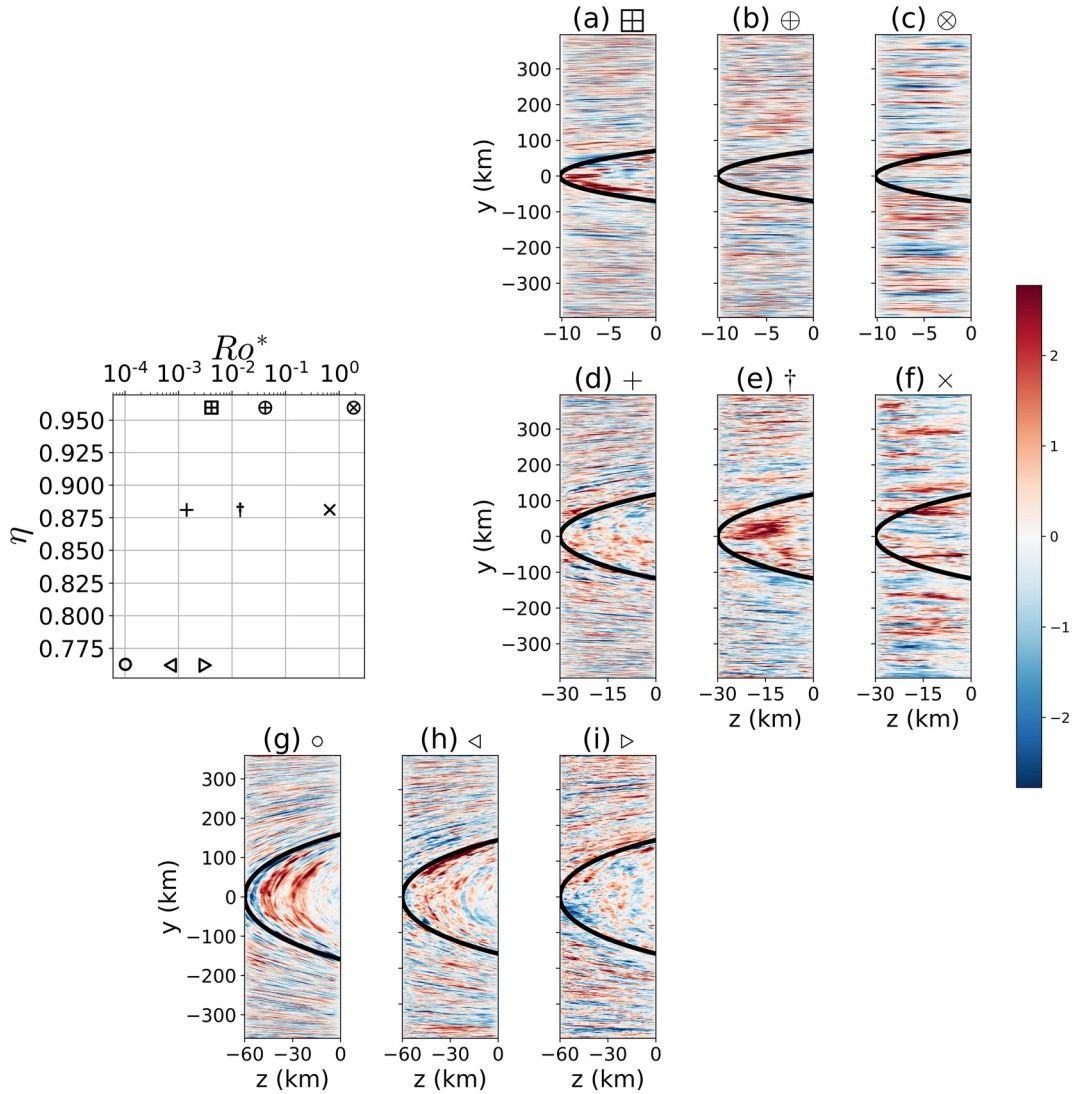

Figure 5. Plots of instantaneous vertical velocity anomalies normalized w.r.t. their standard deviation (see Table 3, $\left(w_{yz} - \overline{w_{yz}}\right) / \widehat{w_{yz}}$ where yz indicates the vertical plane) at $x = 25$ km across our experiments. Here, the overbar represents a mean over the plane and the hat is the standard deviation relative to that mean. The first, second, and third rows represent models with η of 0.96, 0.88, and 0.76, respectively. The natural Rossby number increases toward the right for each row. The tangent cylinder is shown by the horizontal black line.

simulations cluster around these scaling predictions: for $Ro^* < 0.01$ the points broadly follow rotational scaling, while for $Ro^* > 0.01$ the non-rotational scaling is more relevant. Note that Ro^* is not a direct measure of the balance of terms in the momentum equation (inertial vs. Coriolis): it depends on externally imposed macro-properties such as depth, rotation rate and buoyancy flux. We do not expect, therefore, that the transition to rotationally dominated flows occur at $Ro^* = 1$, but rather in the log neighborhood of 1.

Below, we use these results to extrapolate from the parameter regimes of our simulations to those that might pertain on Enceladus and Europa. A comparison to scales proposed by Aurnou et al. (2020), arrived at using a (Ra, E) framework, is given in Appendix A.

4.2.2. Zonal Scale of the Rolls

As a measure of the spatial scales of the rolls, we plot zonal wavenumber spectrums of mid-depth zonal velocity for all experiments and choose the most dominant wavenumbers. The associated wavelengths are scaled by the depth of the ocean and plotted against Ro^* in Figure 9d. We see that when $Ro^* < 0.01$, the zonal length scales of

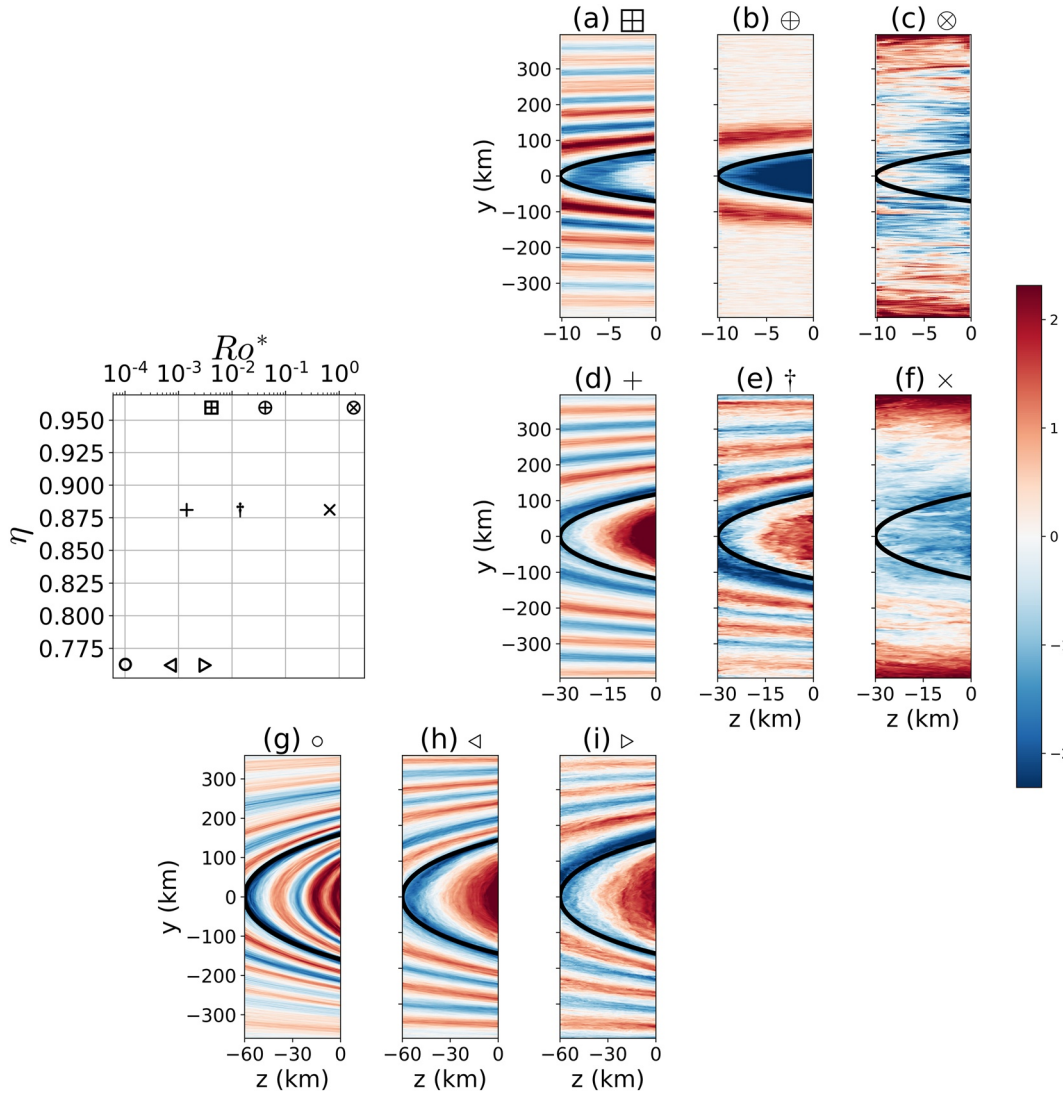

Figure 6. Plots of instantaneous zonal velocity anomalies normalized w.r.t. their standard deviation (see Table 3, $\left(u_{yz} - \overline{u_{yz}}\right) / \widehat{u_{yz}}$ where yz indicates the vertical plane) at $x = 25$ km across our experiments. Here, the overbar represents a mean over the plane and the hat is the standard deviation relative to that mean. The first, second, and third rows represent models with η of 0.96, 0.88, and 0.76, respectively. The natural Rossby number increases toward the right for each row. The tangent cylinder is shown by thick black line.

the rolls broadly covary with l_ρ given by Equation 12, again emphasizing the importance of rotational dynamics. It has previously been shown that, at the onset of convection in rapidly rotating shells, the zonal scale of the rolls increases with decreasing η (Al-Shamali et al., 2004), or equivalently, increasing H. Increasing H indeed results in an increase of the zonal scale of the rolls by the factor $H\,Ro^{*1/2}$. According to Figure 9d, we find that $L \approx 20\,H\,Ro^{*1/2} = 20\,l_\rho$ for the simulations where $Ro^* < 0.01$. This scaling law compares favorably with that derived by equating the vortex stretching and inertial terms in the vorticity budget (Featherstone & Hindman, 2016) and is also close to that presented in Aurnou et al. (2020) and Vasil et al. (2021) where, in the rapidly rotating limit, they suggest $L \sim H\,Ro^{*2/5}$ (see Appendix A for a further discussion).

The physical arguments rehearsed in Section 2.1 suggest that as Ro^* increases the plumes become more radially aligned, thus breaking the Taylor-Proudman constraint and gravity playing a more dominant role. This transition from rotational to gravitational control has important implications for heat transfer across the ocean, as discussed in more detail in Section 4.4.

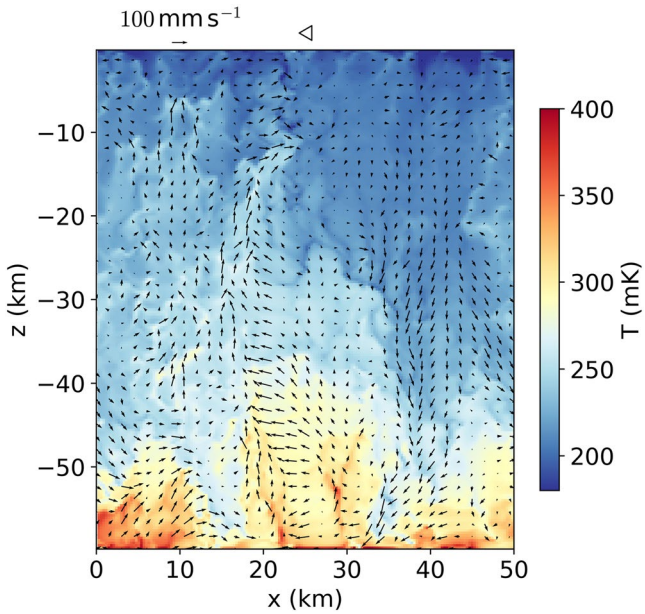

Figure 7. Instantaneous plot of temperature (shading, K) and velocity (arrows) at the equatorial xz-section is shown for experiment ◁. The zonal mean of zonal velocity is subtracted to emphasize the rolls. The downward and upward arrows are accompanied by colder and warmer temperatures, respectively, demonstrating that the ascending and descending arms of the rolls act together to transport heat upwards.

4.2.3. Predicted Turbulent Scales on Enceladus and Europa

Extrapolating from our scaling results in Figure 9, to the parameter regimes possibly occupied by Enceladus and Europa, we can make predictions about the nature of the turbulent scales on these icy moons, assuming that our scaling remains appropriate. Table 4 sets out predicted values for velocity, temperature and length scales on Enceladus and Europa. Following Soderlund (2019), we use two values of H and Q for each moon to encompass likely ranges of these uncertain parameters. It should be noted that heat fluxes on both Enceladus and Europa will likely be much smaller than those used in our experiments. Furthermore, particularly on Enceladus which is purported to be fresher than the ocean on Europa, its thermal expansion coefficient, α, will likely be smaller—see the caption of Table 4. For these reasons the buoyancy fluxes and hence natural Rossby numbers will be very small. Small Rossby numbers in turn mean that our velocity and temperature scales are commensurately smaller: $O\,(0.01-1\text{mm}\,\text{s}^{-1})$ for velocity and $O\,(0.01-0.1\text{mK})$ for temperature. Finally, the deformation radius, l_ρ, is expected to be O $(10-100$ m) and the zonal width of the rolls perhaps 20 times that.

It should be noted, however, that we have prescribed a spatially uniform pattern of bottom heating, whereas one might expect it to be localized, perhaps into stripes, as in the Choblet et al. (2017) study of Enceladus. Local currents and temperature anomalies induced by such localized heat sources would then be very much larger than those set out in Table 4.

4.3. Large-Scale Structure of Zonal Flow and Meridional Temperature Gradients: Thermal Wind Balance and "Rhines Scale"

The mean meridional gradients in temperature are linked to the mean zonal velocity by a generalised thermal wind relationship—(e.g., Aubert, 2005; Aubert et al., 2001; Christensen, 2002; Kaspi et al., 2009, 2018, 2020). Assuming a steady state and neglecting contributions from advective and viscous terms, we set the total derivatives and F terms to zero in the meridional and vertical momentum equations, Equations 16 and 17. The thermal wind relationship is then obtained by eliminating pressure between them to arrive at:

$$f\frac{\partial u}{\partial z}+\frac{\partial\left(\tilde{f}u\right)}{\partial y}=-\frac{\partial b}{\partial y}, \tag{24}$$

where f, $\tilde{f}$ are the vertical and horizontal components of the Coriolis parameter (defined in Equation 19) and b is the buoyancy. Note that the contribution from $\tilde{f}$ is traditionally neglected, yet increasingly dominates outside the tangent cylinder as the equator is approached.

In order to determine the degree of compliance of our experiments with the thermal wind relationship, we first perform a time and zonal average, indicated by $\bar{\cdot}^{x,t}$, of the above equation and integrate in y to obtain a diagnostic relation for b_{TW}, the zonal-mean buoyancy field which would be in thermal wind balance with the zonal-mean zonal velocity field:

$$b_{\text{TW}}(y,z)=\bar{b}^{\,x,t}(y=0,z)-\int_0^y\left(f\frac{\partial\bar{u}^{\,x,t}(y',z)}{\partial z}+\frac{\partial\left(\tilde{f}\bar{u}^{\,x,t}(y',z)\right)}{\partial y'}\right)\mathrm{d}y'. \tag{25}$$

Taking $\bar{b}^{\,x,t}(y=0,z)$ and the interior zonal current from respective model simulations, we integrate Equation 25 in the meridional direction to obtain b_{TW} for each simulation. We then compute the correlation between b_{TW} and the interior buoyancy field, $\bar{b}^{\,x,t}$, taken from the corresponding simulations (excluding top and bottom boundary layers) and plot them as a function of natural Rossby number in Figure 10. We see that experiments with low natural Rossby numbers are in compliance with the thermal wind relationship. Thermal wind becomes less relevant as the influence of rotation diminishes, in agreement with previous studies of Aurnou et al. (2003) and

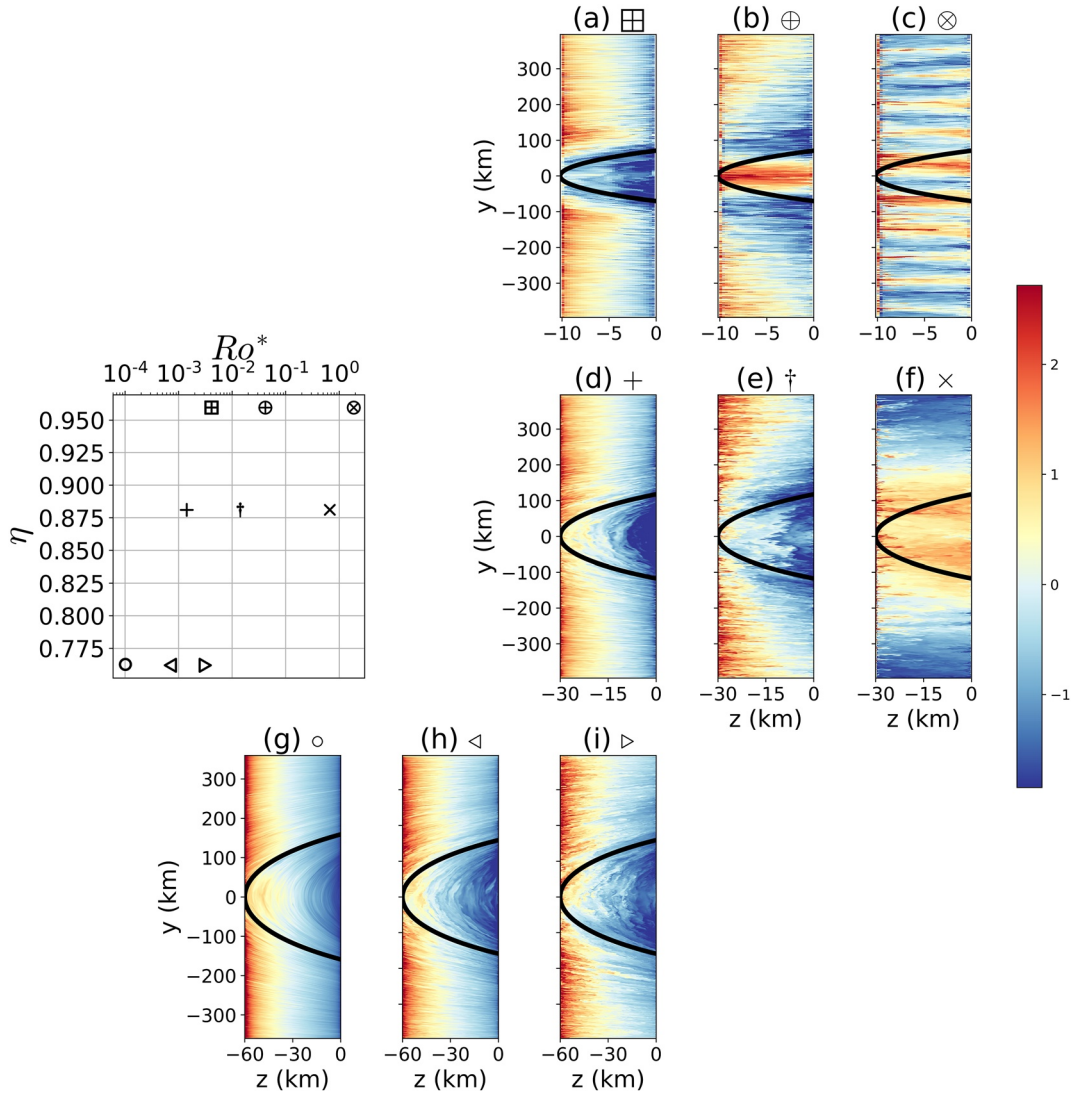

Figure 8. Plots of instantaneous temperature anomalies normalized w.r.t. their standard deviation (see Table 3, $\left(T_{yz} - \overline{T_{yz}}\right)/\widehat{T_{yz}}$ where yz indicates the vertical plane) at $x = 25$ km across our experiments. Here, the overbar represents a mean over the plane and the hat is the standard deviation relative to that mean. The first, second, and third rows represent models with η of 0.96, 0.88, and 0.76, respectively. The natural Rossby number increases toward the right for each row. The tangent cylinder is shown by thick black line.

Aubert (2005) in studies of planetary atmospheres. Since the natural Rossby numbers on Enceladus and Europa are so small, the interior circulation will be in thermal wind balance. In such a scenario, the structure of the zonal flow and temperature found in our models—eastward flow at the upper surface outside the tangent cylinder—is likely to be a feature of the circulation on Enceladus and Europa, if they are primarily driven by heating from below. This is in marked contrast to Soderlund et al. (2013), who predicted westward near-surface flow at the equator of Europa owing to the rather high Rossby number in their simulation (more representative of panel f in Figure 6).

Our experiments with low Rossby numbers comprise multiple alternating zonal currents whose meridional scale might be expected to depend on the "Rhines scale" (Rhines, 1975). On a β-plane the cascade of energy in geostrophic turbulence toward larger scales is arrested by the β-effect, radiated as Rossby waves, and ultimately channeled into zonal jets. Yano et al. (2005) showed that when convection occurs in the presence of Taylor columns aligned along the axis of rotation, the two-dimensional flow in the equatorial plane can reasonably

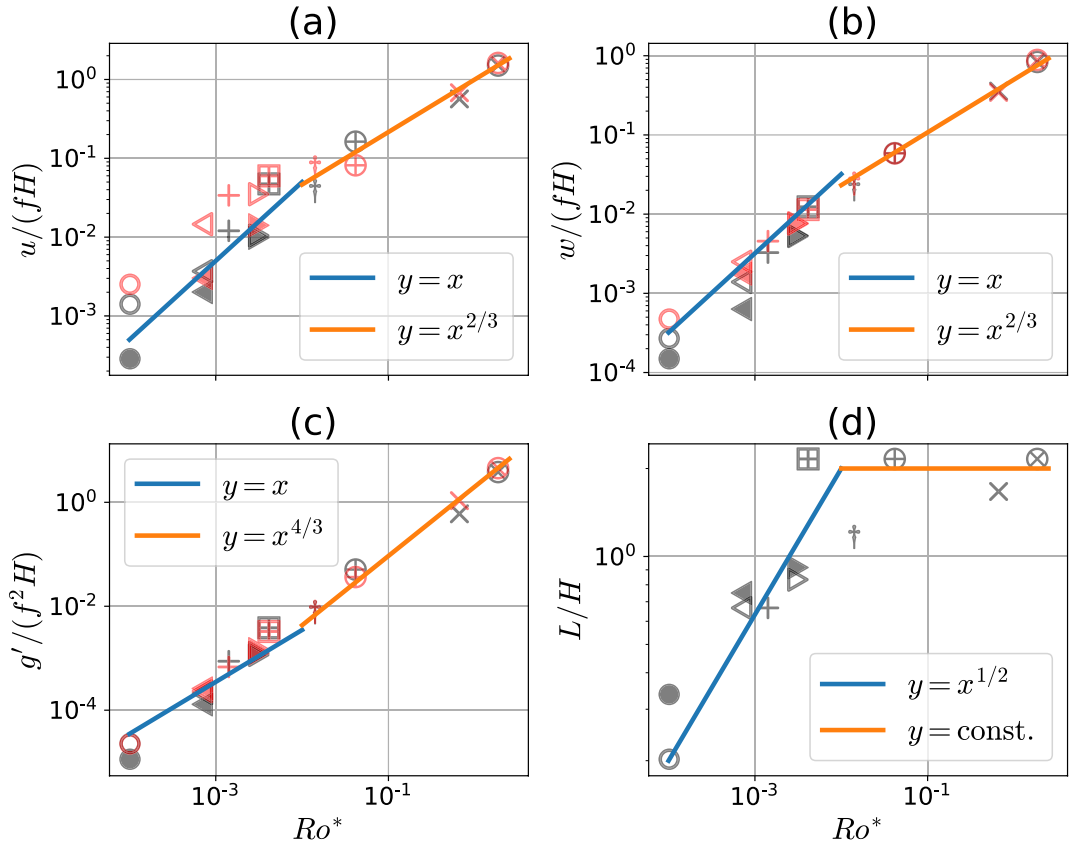

Figure 9. Normalized root mean square ((a) horizontal velocity, (b) vertical velocity, and (c) buoyancy anomaly) at low and high latitudes plotted against natural Rossby number. Black symbols correspond to low latitudes and red symbols high latitudes, where low is defined to be between y = 10 and 50 km, and high between y = 200 and 300 km, respectively. Note that there is no filled red circle on panels (a–c) because this experiment lacks polar plumes (discussed in Section 4.4.1). Panel (d) shows the zonal scale of the rolls, L, normalized by the depth of the domain as a function of natural Rossby number. The blue and orange lines show the theoretical slopes for rotational and non-rotational regimes, respectively.

Table 4
Predictions of Velocity, Temperature, and Deformation Radius Scales for Enceladus and Europa Based on Scalings Shown in Figure 9.

Moon	H (km)	Q (mW m^{-2})	B (10^{-13} m^{2}s^{-3})	Ro^* (10^{-5})	l_ρ (m)	U (mm s^{-1})	W (mm s^{-1})	T' (mK)
Enceladus	11	16	3.9×10^{-2}	0.52	25	0.030	0.019	0.23
	55	16	3.9×10^{-2}	0.1	56	0.030	0.019	0.23
	11	82	2×10^{-1}	1.2	38	0.069	0.044	0.51
	55	82	2×10^{-1}	0.24	85	0.069	0.044	0.51
Europa	97	24	15	4.6	660	0.930	0.600	0.011
	126	24	15	3.5	750	0.930	0.600	0.011
	97	119	72	10.0	980	2.100	1.300	0.025
	126	119	72	7.8	1,100	2.100	1.300	0.025

Note. Following Table 1 of Soderlund (2019), we use two values for ocean depth and heat flux each. The gravity, rotation rate, coefficient of thermal expansion, specific heat capacity, and density on Europa are assumed to be, respectively, 1.3 ms^{-2}, 2.1 $\times$ 10^{-5}s^{-1}, 1.9 $\times$ 10^{-4}K^{-1}, 3,900J kg^{-1}K^{-1}, and 1,040 kg m^{-3}. Those on Enceladus are assumed to be 0.1 ms^{-2}, 5.3 $\times$ 10^{-5}s^{-1}, 1 $\times$ 10^{-5}K^{-1}, 4,000J kg^{-1}K^{-1}, and 1,020 kg m^{-3}.

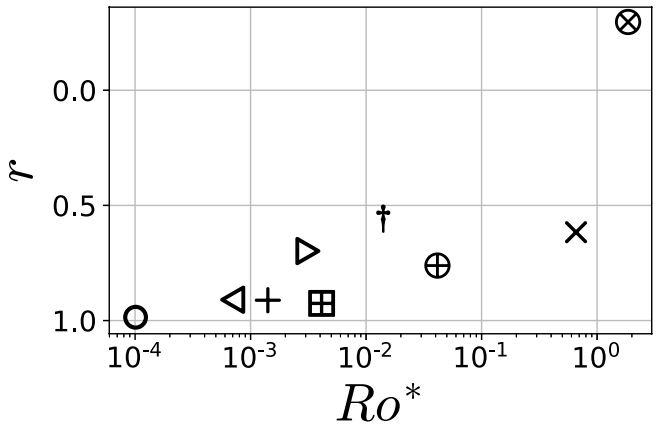

Figure 10. Tests of the thermal wind equation for zonal jets in each of our experiments: the correlation, r, of $\tilde{b}^{x,t}$ with b_{TW} (Equation 25) is plotted as a function of natural Rossby number. The top and bottom 2 km were excluded to avoid boundary layer effects. If the correlation approaches unity then thermal wind balance is increasingly well satisfied.

represent the three-dimensional flow. The topographic β-effect in such a scenario is a consequence of the curvature of the spherical shell. Following Heimpel and Aurnou (2007), we define the Rhines scale as

$$l_\beta = \sqrt{\frac{2U}{\beta}}\frac{1}{\sin\frac{y}{R}}, \tag{26}$$

where

$$\beta = -\frac{2\Omega}{h}\frac{dh}{ds} \tag{27}$$

is the topographic β-effect, h is the height of the Taylor column measured parallel to Ω, s is the radial distance from the rotation axis to the point of intersection of the Taylor column with the outer surface, and U is the speed of the zonal jet. The $\sqrt{2U/\beta}$ term measures the "Rhines scale" of the zonal jets in the equatorial plane. However, since we measure the widths of the jets on the outer shell, they are dilated by a factor $\sin(y/R)^{-1}$.

Figures 11b and 11d compare measured widths with those predicted by the above formula for experiments $\triangleleft$ and $+$, respectively. We find excellent agreement inside the tangent cylinder. Outside, however, the "Rhines scale" underestimates the observed scale of the zonal jets. This departure was also present in Heimpel and Aurnou (2007) where it was attributed to the fact that Taylor columns become almost parallel to the outer shell outside the tangent cylinder and the zonal flows are established due to the drifting of rolls, rather than zonal channeling of energy by Rossby waves. This should be investigated further.

4.4. Latitudinal Dependence of Vertical Heat Transport

We now consider how vertical heat transport, uniform at the bottom, varies with latitude at the upper surface. This is of particular interest because the amount of heat being delivered to the ice shell by the ocean has a tendency to induce freezing/melting and be reflected in the ice-shell thickness, which may therefore be observable. In our model setup, the bottom heat flux is spatially uniform. However, by the time it is transported to the upper boundary it is redistributed by ocean dynamics and exhibits latitudinal dependence. We expect the transition from the "equatorial rolls" to "polar plumes" across the tangent cylinder (see Section 4.1) to be reflected in the heat transport.

To examine this transition, and in the spirit of Amit et al. (2020), in Figure 12a) we plot the ratio

$$q^{\mathrm{h/l}} = \frac{q^{\mathrm{h}} - q^{\mathrm{l}}}{q^{\mathrm{h}} + q^{\mathrm{l}}} \tag{28}$$

against our key non-dimensional number Ro^*. Here

$$q^{\mathrm{l}} = \frac{\int_{-y^{\mathrm{tc}}}^{y^{\mathrm{tc}}}\int q\,\mathrm{d}x\,\mathrm{d}y}{\int_{-y^{\mathrm{tc}}}^{y^{\mathrm{tc}}}\mathrm{d}x\,\mathrm{d}y}, \tag{29}$$

$$q^{\mathrm{h}} = \frac{\int_{y^{\mathrm{tc}}}^{y^{\mathrm{N}}}\int q\,\mathrm{d}x\,\mathrm{d}y}{\int_{y^{\mathrm{tc}}}^{y^{\mathrm{N}}}\mathrm{d}x\,\mathrm{d}y} + \frac{\int_{y^{\mathrm{S}}}^{-y^{\mathrm{tc}}}\int q\,\mathrm{d}x\,\mathrm{d}y}{\int_{y^{\mathrm{S}}}^{-y^{\mathrm{tc}}}\mathrm{d}x\,\mathrm{d}y}, \tag{30}$$

are the spatially averaged heat fluxes inside and outside the tangent cylinder: q is the heat flux in $W\mathrm{m}^{-2}$ at the upper boundary, y^{tc} is the meridional coordinate at which the tangent cylinder intersects the upper surface, and y^{N} and y^{S} are the coordinates of the northern and southern boundaries of the domain, respectively. Positive or negative values of $q^{\mathrm{h/l}}$ indicate polar or equatorial cooling, respectively. Note that the terminology used here is with respect to the ocean. Polar (equatorial) cooling indicates that the polar (equatorial) ocean is losing heat to the ice sheet and therefore cooling.

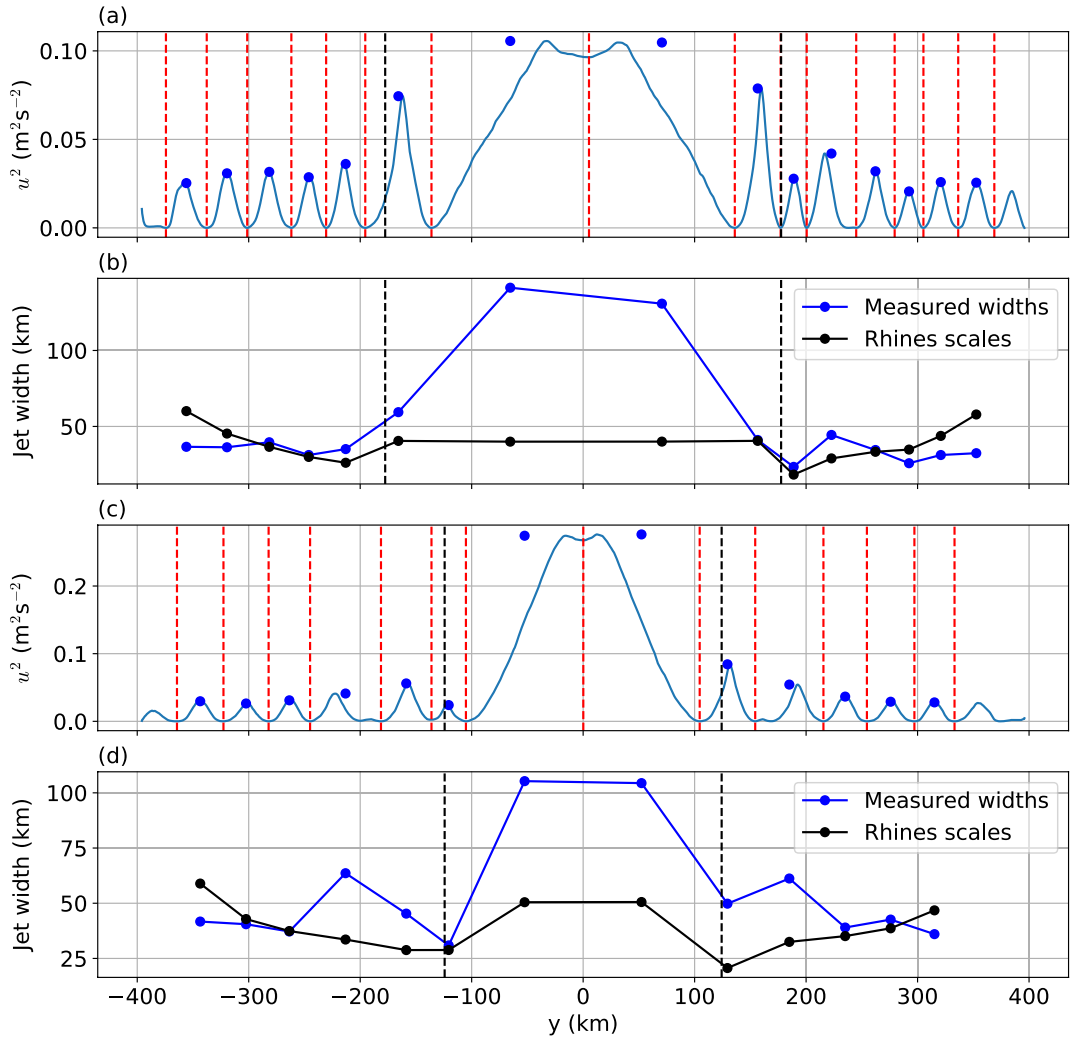

Figure 11. Panels (a and c) show the square of the zonal and time mean surface zonal velocity for experiments ◁ and +, respectively. The meridional locations of the red dashed lines are at the local minima of squared velocity and show the edges of the zonal jets. The meridional locations of the blue dots are at the midpoint of the detected jet edges. The magnitude of the squared velocities indicated by the blue dots is the maximum squared velocity within the confines of the jet. The velocity corresponding to this maximum squared velocity is used as the velocity scale of the jet, U, in Equation 26. Panels (b and d) show the comparison between the Rhines scale, Equation 26, and the measured width of the jets for experiments ◁ and +, respectively. The black dashed lines show the meridional location where the tangent cylinder intersects the outer shell.

4.4.1. Dependence on the Natural Rossby Number

Our nine key experiments show polar cooling at low natural Rossby numbers with a change to uniform cooling at high natural Rossby numbers (see Figure 12a). None exhibit equatorial cooling. Thus, in the presence of significant rotational effects, it appears that plumes rather than rolls are more efficient at carrying heat vertically. As the influence of rotation wanes, meridional variations in vertical heat flux diminish.

This is broadly similar to, but in detail different from, the study of Amit et al. (2020) who find that, in some parameter regimes, equatorial cooling can occur even at small Rossby numbers. They frame the problem in terms of the local Rossby number, $Ro_{\mathrm{loc}} = Ra^{5/4}\,E^2$, and the ratio of the Rayleigh number to a transitional Rayleigh number, $Ra/Ra_{\mathrm{T}} = 0.1\,Ra\,E^{3/2}$. The local Rossby number was proposed by Julien et al. (2012) as a measure of the importance of rotation in the thermal boundary layer. A high local Rossby number indicates that the thermal boundary layer is not rotationally constrained, even though the bulk Rossby number of motions outside the boundary layer could be small. The transitional Rayleigh number corresponds to the condition that the depth of the thermal boundary layer exceeds that of the viscous boundary layer (King et al., 2010). Both Ro_{loc} and Ra/Ra_{T}

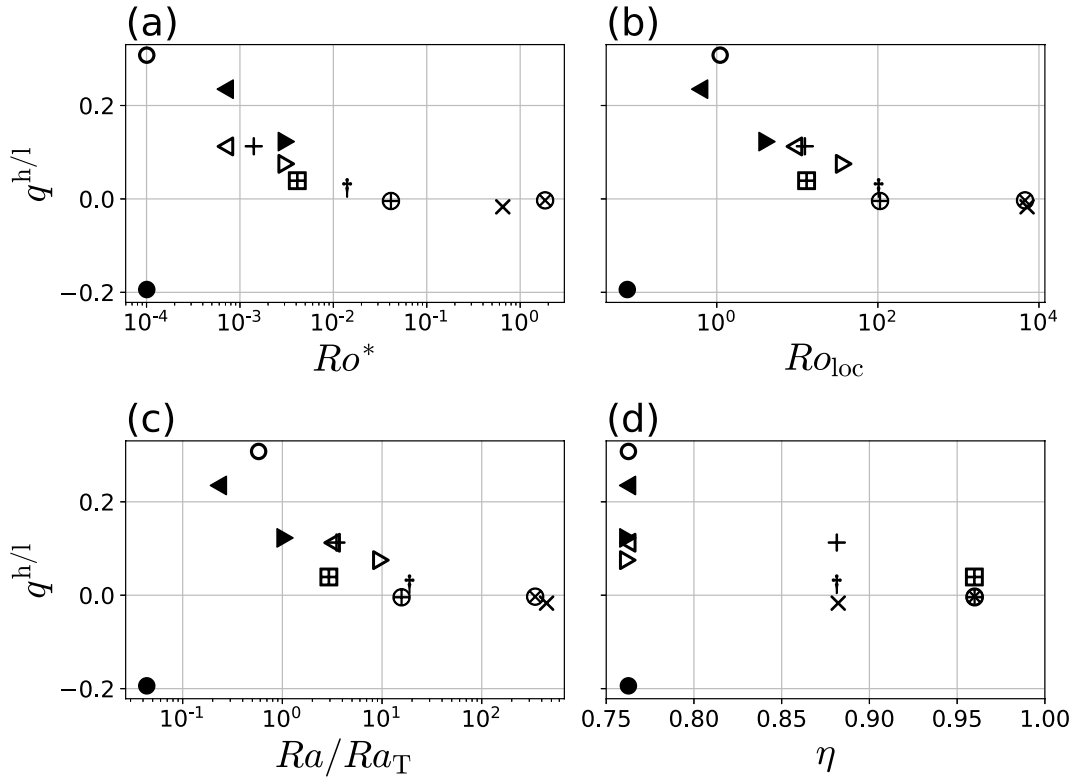

Figure 12. The ratio between high-latitude surface heat flux and low-latitude surface heat flux $q^{h/l}$ from Equation 28 as a function of (a) the natural Rossby number, (b) the local Rossby number, (c) the ratio of Rayleigh number to transitional Rayleigh number, and (d) η. Positive (negative) values of $q^{h/l}$ indicate polar (equatorial) cooling.

can be used to indicate the transition from a rotationally dominant flow regime to a non-rotationally dominant regime. Amit et al. (2020) observe that on increasing Ro_{loc} or, almost equivalently, Ra/Ra_T, there is a regime transition from equatorial cooling to polar cooling and then on to spatially uniform cooling.

To investigate further, we repeat our three low η experiments using exactly the same parameters as before, but using a higher viscosity (see Table A1). The effect of the increased viscosity is to suppress, somewhat, plumy convection within the tangent cylinder, leaving the equatorial rolls to "do more work." By so doing we are able to capture an equatorial cooling regime with a regime transition similar to that found by Amit et al. (2020). As shown in Figures 12b and 12c, at low Ro_{loc} and Ra/Ra_T, the moons tend to lose heat at lower latitudes, at very high Ro_{loc} and Ra/Ra_T heat loss is spatially uniform and, in between, there is a broad intermediate regime with polar cooling.

The natural Rossby number largely captures the pattern of polar cooling and also its plateauing to uniform cooling (Figure 12a), but fails to differentiate between the two lowest Rossby number cases (∘ and •). This happens because increasing viscosity can suppress polar plumes completely, particularly when the bottom heat flux is low (Figures 13a and 14)—the rolls are less susceptible to mixing than the plumes because they are of larger scale. The direction of the meridional heat transport can reverse with increasing viscosity, as shown in Figure 14. It is clear, then, that despite the utility of the natural Rossby number, it cannot provide information about the criticality of the convective system. If plumes are suppressed by viscosity, rolls dominate vertical heat transport resulting in equatorial cooling (e.g., experiment •). Since Ro_{loc} and Ra/Ra_T depend on viscosity, they are able to distinguish between high and low viscosity cases.

The regime diagram suggested by Gastine et al. (2016), plotted in Figure 15, demarcates regions where flow is imagined to be conductive, rotationally dominated, non-rotating, or transitioning between the two. The y-axis is $Ra\ E^{4/3}$, which measures the ratio of Rayleigh number to the critical Rayleigh number (which according to Gastine et al. (2016); Aurnou et al. (2020) scales as $E^{-4/3}$), while the x-axis is the Ekman number. Also plotted on the diagram is a black dashed line proposed by Amit et al. (2020) ($Ra/Ra_T = 1$) to delineate the transition from

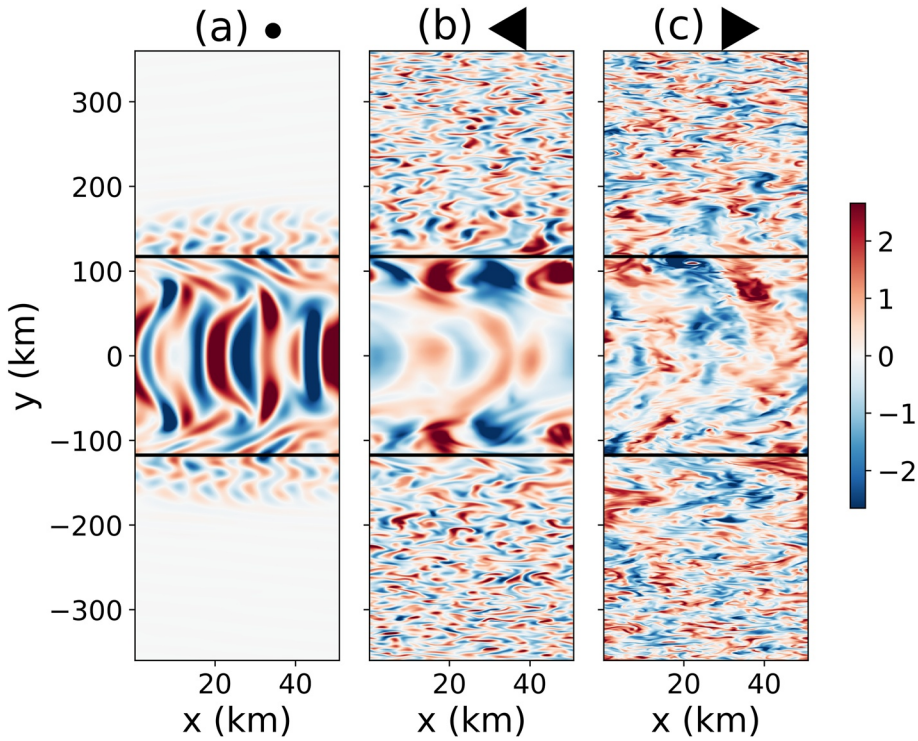

Figure 13. Plots of instantaneous vertical velocity anomalies normalized w.r.t. their standard deviation for reruns of experiments ∘ and ◁ and ▷ in which all parameters are the same except the viscosity and diffusivity have been increased by two orders of magnitude. See Table 2 where these experiments are marked by the black symbols ●, ◀, and ▶. The standard deviations for the three experiments in ms^{-1} are $\widehat{w_{xy}} = \left(1.7 \times 10^{-3}, 1.5 \times 10^{-2}, 6.0 \times 10^{-2}\right)$, respectively.

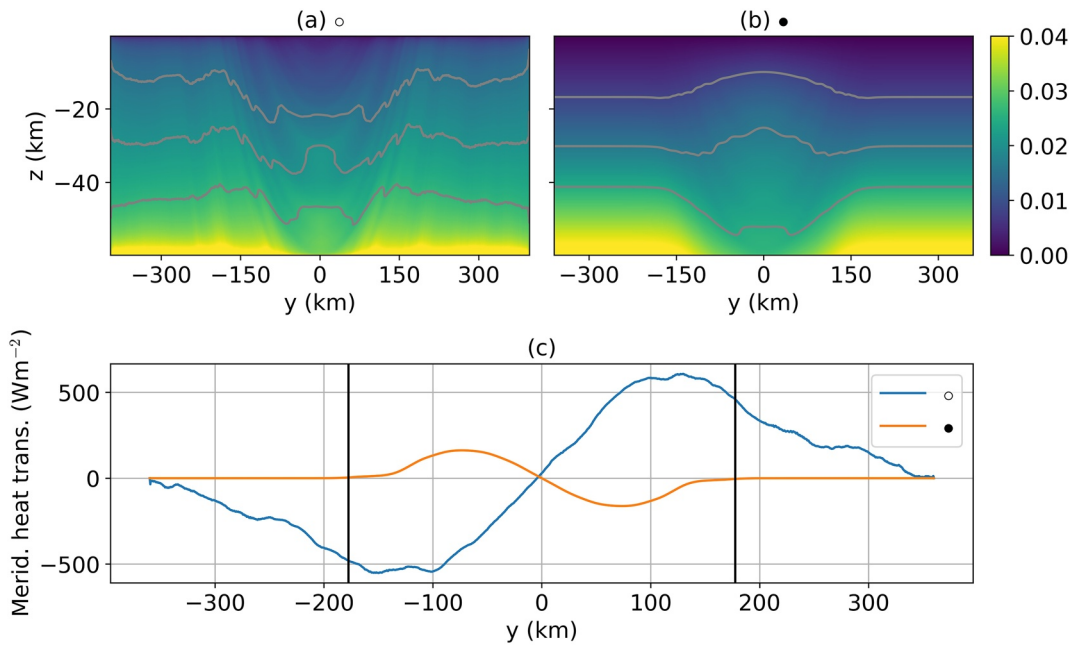

Figure 14. Panels (a and b) show the time and zonal mean temperature in K in experiments ∘ and ●, respectively. Gray lines show the 25th, 50th, and 75th percentiles of time and zonal mean temperature for respective experiments. Panel (c) shows the meridional heat transport as a function of latitude in experiments ∘ and ●. The black lines show the latitudes where the tangent cylinder intersects the surface.

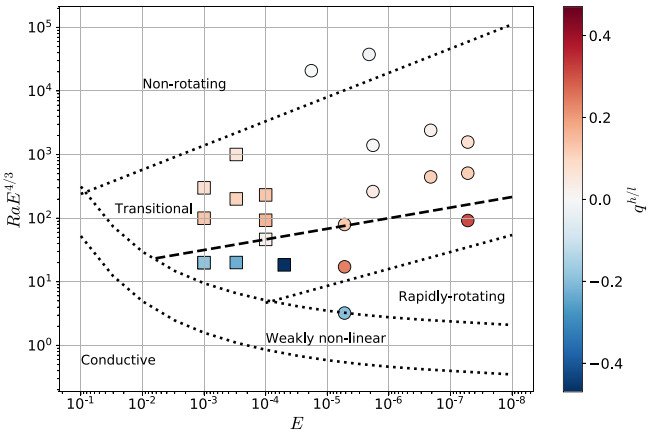

Figure 15. The regime diagram introduced by Gastine et al. (2016) identified by the dotted lines and labels. The y-axis is $Ra\,E^{4/3}$, a measure of the criticality of the flow, and the x-axis is the Ekman number. Experiments carried out in the present study are indicated by circles and those carried out by Amit et al. (2020) by squares. The colors of the squares and circles indicate the value of $q^{h/l}$, red for positive, blue for negative, for which the scale is on the right: red (blue) symbols indicate polar (equatorial) cooling. As discussed in Section 4.4.1, Amit et al. (2020) proposed that the transition from equatorial cooling to polar cooling occurs at $Ra\,E^{3/2} = 10$, plotted as the black dashed line.

equatorial cooling to polar cooling. The observed transition in our experiments (shown by circles in Figure 15) occurs at values of Ro_{loc} and Ra/Ra_{T} that are one order of magnitude smaller than those suggested by Amit et al. (2020). It is for this reason that the dashed line fails to differentiate between equatorial and polar cooling cases in our suite of simulations—three polar cooling cases fall into the equatorial cooling regime proposed by Amit et al. (2020). A more recent study by Hindman et al. (2020) identifies an equatorial convection regime (which they subdivide into "equatorial column" and "modulated" regimes in which polar plumes are suppressed), a "polar cell" regime, and a "polar plume" regime. One of our high viscosity experiments seems to lie in the equatorial convection regime while others lie in the "polar plume" regime.

4.4.2. Effect of η

The ratio of inner to outer radius, η, can also affect heat loss patterns (Figure 12d). As η approaches unity (shallow ocean), the surface heat flux becomes almost uniform irrespective of the natural Rossby number (e.g., experiments ×, ⊗). As η decreases (deep ocean), the heat loss patterns tend to undergo equatorial or polar cooling depending on the magnitude of heat flux and viscosity. This pattern arises because at high η the oceans are very shallow which makes it easy for heat to transit across the water column in relatively short time without much meridional transport. On the other hand, the greater depth of the oceans at low η facilitates meridional transport of heat. The overall picture that emerges from our experiments is that the rotational regime, characterized by low natural Rossby number, can exhibit both polar and equatorial cooling. The experiments that resolve plumes tend to support polar cooling. In experiments in which plumes are suppressed, for example, due to high viscosity, equatorial rolls are more efficient in transporting heat. We imagine that the boundary between polar and equatorial cooling might be blurry and depend upon the Ekman number (Hindman et al., 2020). This indicates that the role of unresolved turbulence cannot be ignored in establishing the meridional pattern of cooling.

4.4.3. Predictions for Enceladus and Europa

Despite all the above caveats, we cannot resist but to speculate on the implications of our results for icy moons. Europa has ($Ro^* \sim 10^{-4}$ and $\eta \sim 0.93$), and Enceladus has ($Ro^* \sim 10^{-6}$ and $\eta \sim 0.83$; see Table A1). With such low natural Rossby numbers both are expected to be under rotational control, and thus $q^{h/l}$ will deviate from one. Because of somewhat larger η, Europa's ocean may lose heat almost uniformly over the globe. Enceladus has a considerably smaller η, however, and so perhaps has prominent meridional heat transport. Whether equatorial cooling or polar cooling dominates will depend on the eddy viscosity/diffusivity of the Enceladean ocean. Previous studies tend to use molecular values of viscosity and diffusivity to locate natural icy moons in Rayleigh-Ekman space. However, according to Rekier et al. (2019), the libration of Enceladus could generate much turbulence, significantly elevating fluid viscosities and diffusivities above molecular values. According to the estimate in Kang et al. (2021), the turbulent viscosity of Enceladus' ocean might be as high as $O\left(10^{-3}\mathrm{m}^2\mathrm{s}^{-1}\right)$. This places Enceladus in the rapidly rotating regime in Gastine's regime diagram, Figure 15. Due to limited computational resources, we cannot integrate experiments out to equilibrium with a realistic heat flux (three orders magnitude smaller than the lowest heat flux employed here), and we do not yet have enough experiments to identify a universal scaling law. It remains unclear to us, therefore, what form the meridional profile of heat loss will take on a hypothetical Enceladus heated only from below.

5. Summary and Discussion

We have explored and attempted to rationalize the ocean dynamics and heat transport on icy moons heated uniformly from below using a set of high-resolution large eddy simulations. We do not consider the role of salt, except in so far as we assume that the coefficient of thermal expansion of water is positive, appropriate if the ocean is sufficiently salty. Departing from previous studies, we have organized our experiments in terms of the natural Rossby number, Ro^*, and the ratio of the inner to the outer radius of the ocean, η, which controls the geometry of the tangent cylinder. Rather than set a temperature difference across the fluid, we have prescribed a bottom heat

flux and relaxed temperature at the top to the freezing point of water. Finally, we have adopted a novel dynamical and modeling framework—that of a non-traditional β-plane running at high resolution on GPUs—allowing us to simultaneously resolve turbulent and large-scale circulations. This has enabled us to explore parameter space and perhaps approach more realistic regimes than in previous studies.

Our main findings are:

1. Rather simple scaling laws based on Ro^*, inspired by early work on open ocean deep convection reviewed in Marshall and Schott (1999), usefully collapse velocity and temperature scales. Turbulent velocities and temperatures scale with u_{rot}, T_{rot} and u_{norot}, T_{norot} in, respectively, low and high Ro^* regimes. In the low Ro^* limit, typical of most icy moons and particularly Enceladus and Europa, the circulation will be under strong rotational control and Taylor column behavior. This has been the subject of many studies on convection in rotating spherical shell applied to planetary atmospheres, Earth's core, and early Earth's magma ocean (see for e.g., Aubert, 2005; Aurnou et al., 2003; Cardin & Olson, 1994; F. Busse & Cuong, 1977; Gastine et al., 2016; Kaspi et al., 2018, 2020; Maas & Hansen, 2019; Miquel et al., 2018).
2. All simulations, except those with Ro^* in excess of ∼0.1, display two regions of circulation demarcated by the tangent cylinder, characterized by the geometrical parameter η. Inside the tangent cylinder (high latitudes), rotationally modified convective "plumes" dominate (Aurnou et al., 2008; Gastine et al., 2016; Hindman et al., 2020); they shoot upward parallel to the rotation axis along Taylor columns that reach from the bottom to the ice shell. Outside the tangent cylinder (low latitudes), Taylor columns do not intersect the bottom and "rolls" dominate (Al-Shamali et al., 2004; Aubert, 2005; Aurnou et al., 2003); they swirl in the equatorial plane about the direction of rotation. An appropriately defined deformation radius, which scales with Ro^*, sets the zonal scales of the equatorial rolls.
3. When Ro^* is small, geostrophic turbulence is excited by convection bubbling up from below. This, in turn, energizes alternating zonal jets (Aurnou et al., 2007, 2008; Manneville & Olson, 1996) whose meridional width is consistent with the "Rhines scale" based on the topographic β of the spherical shell and the speed of the jet. The "Rhines scale" successfully predicts the width of the zonal jets inside the tangent cylinder but underestimates their width outside it (Heimpel & Aurnou, 2007). The zonal jets are found to be in thermal wind balance for experiments with low Rossby numbers (Aubert, 2005; Aurnou et al., 2003).
4. The efficiency of vertical heat transport varies with latitude because of the different dynamics inside and outside the tangent cylinder. In the limit that Ro^* is small, the heat flux to the ice shell might be expected to be weaker in the tropics, because the tangent cylinder creates a "forbidden zone" that prevents Taylor columns extending from the seafloor to the ice shell (Aurnou et al., 2008; Vance & Goodman, 2009). Although this is generally observed in our experiments, whether heat will be lost more to the equatorial or polar ice shell cannot be convincingly predicted by consideration of the mixing-independent Ro^* alone. This is because increasing diffusivity/viscosity preferentially damps small-scale higher-latitude plumes in favor of larger-scale equatorial rolls, thus promoting equatorial cooling (Hindman et al., 2020). We examined the efficacy of the non-dimensional numbers Ro_{loc} and Ra/Ra_{T}, in explaining the relative heat transport efficiency in low and high latitudes. Both provide a useful qualitative rationalization but do not quantitatively frame both our results and those of Amit et al. (2020).
5. The relative heat transport efficiency of low versus high latitudes also depends on the geometrical parameter η. When the ocean is shallow, the heat flux is increasingly dominated by the radial component and does not strongly depend on latitude. In contrast, when the ocean is deep, meridional transport of heat occurs which depends on the relative efficiency of plumes and rolls in heat transport. We have yet to identify a universal scaling law for meridional versus vertical heat transport and its dependence on latitude. This calls for further numerical and theoretical studies.
6. Identification of key non-dimensional numbers enables us to extrapolate to conditions on Enceladus and Europa, and make predictions about what their circulation might look like. As anticipated by the arguments in, for example, Vance and Goodman (2009) and advanced through numerical simulation here, we expect these moons to have a "Jovian-like" circulation: an unstratified, turbulent, geostrophically controlled ocean with strong "Taylor column" behavior and a global circulation dominated by counter-rotating zonal jets. This stands in contrast to the modeling results of Soderlund et al. (2013) for Europa and is in closer agreement with the recent study of Ashkenazy and Tziperman (2021) simulations of Europa. The current study provides the theoretical underpinning from which to interpret these studies.

In summary, we have attempted to draw together and apply to icy moons two distinct world views, one rooted in terrestrial oceanography, the other in exploration of convection on the gas giants and stars. Much can be learned by comparing notes.

Appendix A: Interpretation in Terms of Rayleigh Number and Ekman Number Space

The body of our paper repeatedly extols the natural Rossby number, Ro^*, as the organizing principle from which to view the dynamics of icy moons. Here, we attempt to briefly connect our study to the classical literature of rotating convection between two flat parallel plates across which an adverse temperature difference is prescribed. The ensuing convection is controlled by the Rayleigh number, Ra, and Ekman number, E, (or equivalently the Taylor number Ta), defined by:

$$Ra \equiv \frac{\alpha g \Delta T H^3}{\nu \kappa} \tag{A1}$$

$$Ta \equiv \frac{1}{E^2}, \quad E \equiv \frac{\nu}{2\Omega H^2}, \tag{A2}$$

where ν and κ are the viscosity and diffusivity of the fluid, respectively. If the fluid carries a heat flux Q between the plates, then the Nusselt number,

$$Nu \equiv \frac{QH}{\rho_{\mathrm{ref}} C_{\mathrm{p}} \kappa \Delta T}, \tag{A3}$$

is a convenient measure of the ratio of the total heat transported between the plates to the conductive heat transport. Turbulent convection occurs at highly super-critical Rayleigh numbers in which the Ekman number is very small: the resulting Nusselt number is large because the heat flux carried by turbulent convection dominates the conductive flux.

Using this framework, Boubnov and Golitsyn (1990); Julien et al. (2012); Stellmach et al. (2014); Ecke and Niemela (2014); Gastine et al. (2016); Cheng et al. (2018); Soderlund (2019); Amit et al. (2020); and Kunnen (2021) for example, among many others, employ a regime diagram that divides the (Ra, E) plane into differing dynamical regimes. We made use of one such regime diagram, due to Gastine et al. (2016), in Figure 15. Lines on this diagram delineate the transition from, for example, the conductive regime to the weakly non-linear regime, etc., on to the non-rotating regime. However, there is a rather unsatisfactory aspect of the (Ra, E) pairing. Each depends on the viscosity and diffusivity, which in most real geophysical applications must be interpreted as eddy viscosities and diffusivities. These are often taken to be the same (Prandtl number, Pr = 1), are likely much larger than molecular values, but are rather poorly constrained by observations, if at all, and very challenging to model.

Table A1
Various Non-Dimensional Numbers Estimated From the Simulations Performed in Our Study

	H (km)	Q (W m^{-2})	η	$Ro^* \times 10^{-5}$	$Ra \times 10^{10}$	$Ra^* \times 10^{-4}$	$Ra^*_{\mathrm{q}} \times 10^{-7}$	$E \times 10^{-8}$	$Nu^* \times 10^{-6}$	$Nu \times 10^{3}$	Ro_{loc}	Ra/Ra_{T}
⊞	10	500	0.96	410	1.2	390	170	180	420	0.23	13	2.9
⊕	10	50,000	0.96	4,100	6.3	2,100	1.7×10^4	180	7,900	4.4	100	15.4
⊗	10	100,000	0.96	1.8×10^5	4.4	1.4×10^5	3.3×10^7	1,800	2.3×10^5	13	6.6×10^3	338
+	30	500	0.88	140	36	160	19	21	120	0.58	12	3.4
†	30	50,000	0.88	1,400	190	850	1,900	21	2,200	11	100	18.5
×	30	100,000	0.88	6.2×10^4	140	6.2×10^4	3.8×10^6	210	6.2×10^4	30	6.7×10^3	425
∘	60	10	0.76	9.8	47	13	9.5×10^{-2}	5.2	7.4	0.14	1.1	0.56
◁	60	500	0.76	69	260	71	4.8	5.2	67	1.3	9.1	3.1
▷	60	10,000	0.76	310	800	220	95	5.2	430	8.3	37	9.6
•	60	10	0.76	9.8	3.5×10^{-3}	9.7	9.5×10^{-2}	520	9.8	1.9×10^{-3}	7.5×10^{-2}	0.04
◀	60	500	0.76	69	1.9×10^{-2}	52	4.8	520	92	1.8×10^{-2}	0.61	0.23
▶	60	10,000	0.76	310	8.7×10^{-2}	240	95	520	400	7.6×10^{-2}	4.1	1.0

Note. The temperature difference, ΔT, required to calculate Ra, Ra^*, and Nu was diagnosed from the experiments by performing a horizontal and time mean and taking the difference of temperature between the top and bottom.

In fully developed turbulent convection, one might expect the dependence of viscosity and diffusivity to become weaker and weaker. Indeed regime transitions have been suggested which depend on some combination of (Ra, E), in which the dependence on viscosity and diffusivity largely cancel out, leaving scaling results which depend only on external parameters, such as those that make up the natural Rossby number, Ro*, of Jones and Marshall (1993) and Maxworthy and Narimousa (1994). For example, Christensen (2002); Christensen and Aubert (2006); and Aurnou et al. (2020) identify a modified flux Rayleigh number Ra_q^*:

$$Ra_\mathrm{q}^* \equiv \frac{\alpha g \overline{Q}}{\rho_\mathrm{ref} C_\mathrm{p} \Omega^3 H^2}. \tag{A4}$$

which, it turns out, is exactly equivalent to Ro*: in fact, $\mathrm{Ra}_\mathrm{q}^* = Ro^{*2}$. In the asymptotic regime approached at sufficiently small Ekman numbers, Christensen (2002) and Christensen and Aubert (2006) find that:

$$Ro_\mathrm{H} \equiv \frac{U}{\Omega H} = 3.0 \left(Ra_\mathrm{q}^*\right)^{1/5}, \tag{A5}$$

$$Nu^* \equiv \frac{Q}{\rho_\mathrm{ref} C_\mathrm{p} \Delta T \Omega H} = 0.077 \left(Ra_\mathrm{q}^*\right)^{5/9}. \tag{A6}$$

where the Rossby number, Ro_H, characterizes the importance of advection and inertia relative to rotation, and the Nusselt-like number, Nu*, is obtained by setting $\kappa = \Omega H^2$ in Equation A3.

For completeness we compare our experiments with the above scaling laws in Figure A1. In panel a, the low modified flux Rayleigh number runs (dashed lines) asymptotically approach the theoretical curve (solid line) with increasing Ra_q^*. This is predicted by Christensen (2002) arguing that the effect of viscous forces decreases with increasing flux Rayleigh number. As shown in panel b, our experiments also fall onto the theoretical line Equation A6. It should be noted that the constants of proportionality are different from those in previous studies, which we attribute to differences in model setups. Finally, a recent study by Aurnou et al. (2020) stresses the importance of the convective Rossby number defined by

$$Ro_\mathrm{c} = \sqrt{\frac{Ra\, E^2}{\mathrm{Pr}}}, \tag{A7}$$

where Pr is the Prandtl number. They argue that in the rapidly rotating, inviscid limit, the following length, velocity, and buoyancy scales ought to emerge:

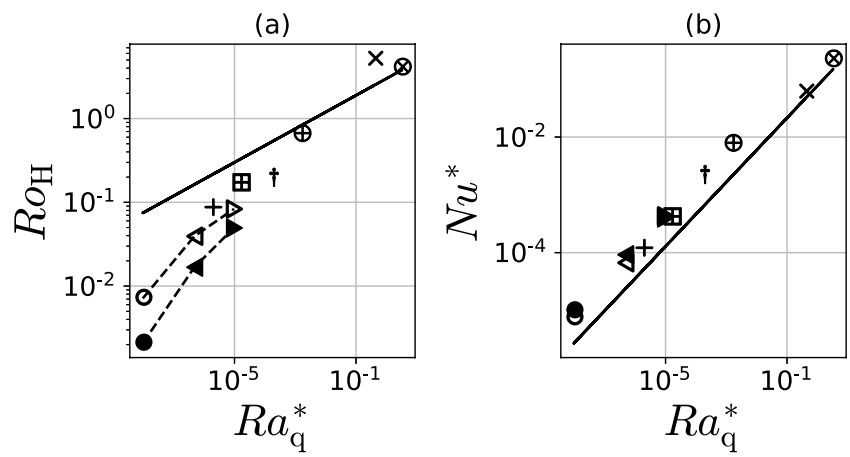

Figure A1. (a) The prediction of Christensen (2002), Equation A5, is plotted by the solid line. The symbols and connecting dashed lines are estimates of Ro_H and Ra_q^* from our numerical experiments. (b) The solid line represents the theoretical scaling between Nu* and Ra_q^*, Equation A6. The symbols represent the positions of our numerical experiments in this phase space. Note that $\mathrm{Ra}_\mathrm{q}^* = Ro^{*2}$.

$$\frac{l}{H} \sim Ro_c;\ \frac{u}{fH} \sim {Ro_c}^2;\ \frac{g'}{f^2H} \sim {Ro_c}^3, \tag{A8}$$

where $Ro_c \sim Ro^{*2/5}$. Expressed in terms of the natural Rossby number, these scales become:

$$\frac{l}{H} \sim Ro^{*2/5};\ \frac{u}{fH} \sim Ro^{*4/5};\ \frac{g'}{f^2H} \sim Ro^{*6/5}. \tag{A9}$$

It is encouraging that these predictions are not significantly different from the l_{rot}, u_{rot}, and g'_{rot} scales discussed in Section 2.2.1 of our study—see Figure A2 where they are compared. Scales for the non-rotating limit are unchanged from the l_{norot}, u_{norot}, and g'_{norot} scales.

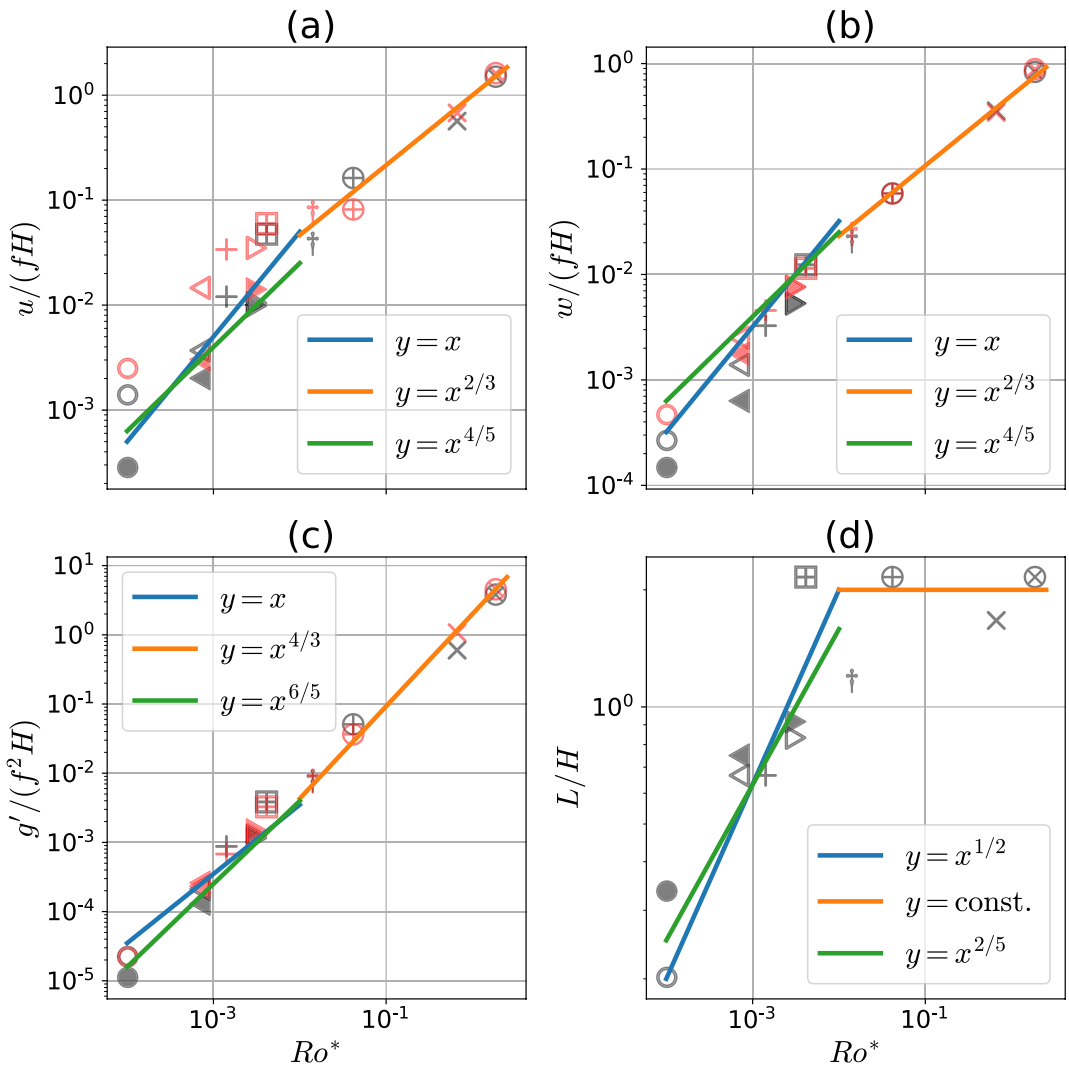

Figure A2. The black and red symbols show the normalized root mean square quantities ((a) horizontal velocity, (b) vertical velocity, and (c) buoyancy anomaly) for low- and high-latitudes, respectively, as functions of natural Rossby number. Root mean square quantities for low and high latitude regions are calculated between $y = 10$ and 50 km, and $y = 200$ and 300 km, respectively. Panel (d) shows the zonal scale of the rolls, L, normalized by the depth of the domain as a function of natural Rossby number. The blue and orange lines show the theoretical slopes for rotational and non-rotational regimes from our study, respectively. The green lines show the theoretical slopes for rotational regime predicted by (Aurnou et al., 2020).

Data Availability Statement

The data used in this study is provided at Bire (2021) and the specific version of Oceananigans used for this study is archived at Ramadhan et al. (2021).

Acknowledgments
The authors would like to thank the NASA Astrobiology Grant 80NSSC19K1427 "Exploring Ocean Worlds" (https://oceanworlds.whoi.edu/exploring-ocean-worlds/) project for funding this research and providing regular feedback. W. Kang would like to thank the Lorenz/Houghton fellowship at MIT for supporting her. S. Bire would like to thank Oliver Jahn for help with model setup and analysis. Computational resources for this project were supplied by Svante and Satori clusters at MIT. The authors also thank Jason Goodman, together with an anonymous reviewer, for many insightful and helpful comments which helped us improve our study and its presentation.

References

Al-Shamali, F., Heimpel, M., & Aurnou, J. (2004). Varying the spherical shell geometry in rotating thermal convection. *Geophysical & Astrophysical Fluid Dynamics*, *98*(2), 153–169. https://doi.org/10.1080/03091920410001659281

Amit, H., Choblet, G., Tobie, G., Terra-Nova, F., Čadek, O., & Bouffard, M. (2020). Cooling patterns in rotating thin spherical shells — Application to Titan's subsurface ocean. *Icarus*, *338*, 113509. https://doi.org/10.1016/j.icarus.2019.113509

Arakawa, A., & Lamb, V. R. (1977). Computational design of the basic dynamical processes of the UCLA general circulation model. In J. Chang (Ed.), *General circulation models of the atmosphere* (Vol. 17, pp. 173–265). Elsevier. https://doi.org/10.1016/B978-0-12-460817-7.50009-4

Ashkenazy, Y., & Tziperman, E. (2021). Dynamic Europa ocean shows transient Taylor columns and convection driven by ice melting and salinity. *Nature Communications*, *12*(1). https://doi.org/10.1038/s41467-021-26710-0

Aubert, J. (2005). Steady zonal flows in spherical shell dynamos. *Journal of Fluid Mechanics*, *542*(-1), 53. https://doi.org/10.1017/s0022112005006129

Aubert, J., Brito, D., Nataf, H.-C., Cardin, P., & Masson, J.-P. (2001). A systematic experimental study of rapidly rotating spherical convection in water and liquid gallium. *Physics of the Earth and Planetary Interiors*, *128*(1–4), 51–74. https://doi.org/10.1016/s0031-9201(01)00277-1

Aurnou, J., Andreadis, S., Zhu, L., & Olson, P. (2003). Experiments on convection in Earth's core tangent cylinder. *Earth and Planetary Science Letters*, *212*(1–2), 119–134. https://doi.org/10.1016/s0012-821x(03)00237-1

Aurnou, J., Heimpel, M., Allen, L., King, E., & Wicht, J. (2008). Convective heat transfer and the pattern of thermal emission on the gas giants. *Geophysical Journal International*, *173*(3), 793–801. https://doi.org/10.1111/j.1365-246x.2008.03764.x

Aurnou, J., Heimpel, M., & Wicht, J. (2007). The effects of vigorous mixing in a convective model of zonal flow on the ice giants. *Icarus*, *190*(1), 110–126. https://doi.org/10.1016/j.icarus.2007.02.024

Aurnou, J., Horn, S., & Julien, K. (2020). Connections between nonrotating, slowly rotating, and rapidly rotating turbulent convection transport scalings. *Physical Review Research*, *2*(4), 043115. https://doi.org/10.1103/physrevresearch.2.043115

Besard, T., Foket, C., & De Sutter, B. (2019). Effective extensible programming: Unleashing Julia on GPUs. *IEEE Transactions on Parallel and Distributed Systems*, *30*(4), 827–841. https://doi.org/10.1109/TPDS.2018.2872064

Bezanson, J., Edelman, A., Karpinski, S., & Shah, V. B. (2017). Julia: A fresh approach to numerical computing. *SIAM Review*, *59*(1), 65–98. https://doi.org/10.1137/141000671

Bire, S. (2021). JuicyMoonsLongChannel [Data set]. Zenodo. https://doi.org/10.5281/zenodo.5228689

Borucki, J. G., Khare, B., & Cruikshank, D. P. (2002). A new energy source for organic synthesis in Europa's surface ice. *Journal of Geophysical Research*, *107*(E11), 24-1–24-5. https://doi.org/10.1029/2002je001841

Boubnov, B. M., & Golitsyn, G. S. (1990). Temperature and velocity field regimes of convective motions in a rotating plane fluid layer. *Journal of Fluid Mechanics*, *219*(-1), 215. https://doi.org/10.1017/s0022112090002920

Brown, D. L., Cortez, R., & Minion, M. L. (2001). Accurate projection methods for the incompressible Navier–Stokes equations. *Journal of Computational Physics*, *168*(2), 464–499. https://doi.org/10.1006/jcph.2001.6715

Busse, F., & Cuong, P. (1977). Convection in rapidly rotating spherical fluid shells. *Geophysical & Astrophysical Fluid Dynamics*, *8*(1), 17–41. https://doi.org/10.1080/03091927708240369

Busse, F. H. (1970). Thermal instabilities in rapidly rotating systems. *Journal of Fluid Mechanics*, *44*(3), 441–460. https://doi.org/10.1017/s0022112070001921

Calkins, M. A., Hale, K., Julien, K., Nieves, D., Driggs, D., & Marti, P. (2015). The asymptotic equivalence of fixed heat flux and fixed temperature thermal boundary conditions for rapidly rotating convection. *Journal of Fluid Mechanics*, *784*, R2. https://doi.org/10.1017/jfm.2015.606

Cardin, P., & Olson, P. (1992). An experimental approach to thermochemical convection in the Earth's core. *Geophysical Research Letters*, *19*(20), 1995–1998. https://doi.org/10.1029/92gl01883

Cardin, P., & Olson, P. (1994). Chaotic thermal convection in a rapidly rotating spherical shell: Consequences for flow in the outer core. *Physics of the Earth and Planetary Interiors*, *82*(3–4), 235–259. https://doi.org/10.1016/0031-9201(94)90075-2

Cheng, J. S., Aurnou, J. M., Julien, K., & Kunnen, R. P. J. (2018). A heuristic framework for next-generation models of geostrophic convective turbulence. *Geophysical & Astrophysical Fluid Dynamics*, *112*(4), 277–300. https://doi.org/10.1080/03091929.2018.1506024

Choblet, G., Tobie, G., Sotin, C., Běhounková, M., Čadek, O., Postberg, F., & Souček, O. (2017). Powering prolonged hydrothermal activity inside Enceladus. *Nature Astronomy*, *1*(12), 841–847. https://doi.org/10.1038/s41550-017-0289-8

Christensen, U. R. (2002). Zonal flow driven by strongly supercritical convection in rotating spherical shells. *Journal of Fluid Mechanics*, *470*, 115–133. https://doi.org/10.1017/s0022112002002008

Christensen, U. R., & Aubert, J. (2006). Scaling properties of convection-driven dynamos in rotating spherical shells and application to planetary magnetic fields. *Geophysical Journal International*, *166*(1), 97–114. https://doi.org/10.1111/j.1365-246x.2006.03009.x

Deardorff, J. W. (1980). Stratocumulus-capped mixed layers derived from a three-dimensional model. *Boundary-Layer Meteorology*, *18*(4), 495–527. https://doi.org/10.1007/bf00119502

Dellar, P. J. (2011). Variations on a beta-plane: Derivation of non-traditional beta-plane equations from Hamilton's principle on a sphere. *Journal of Fluid Mechanics*, *674*, 174–195. https://doi.org/10.1017/s0022112010006464

Dormy, E., Soward, A. M., Jones, C. A., Jault, D., & Cardin, P. (2004). The onset of thermal convection in rotating spherical shells. *Journal of Fluid Mechanics*, *501*, 43–70. https://doi.org/10.1017/s0022112003007316

Dowling, T. E. (1995). Dynamics of Jovian atmospheres. *Annual Review of Fluid Mechanics*, *27*(1), 293–334. https://doi.org/10.1146/annurev.fl.27.010195.001453

Ecke, R. E., & Niemela, J. J. (2014). Heat transport in the geostrophic regime of rotating Rayleigh-Bénard convection. *Physical Review Letters*, *113*(11), 114301. https://doi.org/10.1103/physrevlett.113.114301

Evonuk, M., & Glatzmaier, G. A. (2006). Modeling convection and zonal winds in giant planets. *Proceedings of the International Astronomical Union*, *2*(S239), 177–187. https://doi.org/10.1017/s1743921307000397

Featherstone, N. A., & Hindman, B. W. (2016). The emergence of solar supergranulation as a natural consequence of rotationally constrained interior convection. *The Astrophysical Journal*, *830*(1), L15. https://doi.org/10.3847/2041-8205/830/1/l15

Fernando, H. J. S., Chen, R.-R., & Boyer, D. L. (1991). Effects of rotation on convective turbulence. *Journal of Fluid Mechanics*, *228*, 513. https://doi.org/10.1017/s002211209100280x

Gastine, T., Wicht, J., & Aubert, J. (2016). Scaling regimes in spherical shell rotating convection. *Journal of Fluid Mechanics*, *808*, 690–732. https://doi.org/10.1017/jfm.2016.659

Grimshaw, R. H. J. (1975). A note on the β-plane approximation. *Tellus*, *27*(4), 351–357. https://doi.org/10.3402/tellusa.v27i4.9982

Guervilly, C., & Cardin, P. (2017). Multiple zonal jets and convective heat transport barriers in a quasi-geostrophic model of planetary cores. *Geophysical Journal International*, *211*(1), 455–471. https://doi.org/10.1093/gji/ggx315

Hand, K., & Chyba, C. (2007). Empirical constraints on the salinity of the European ocean and implications for a thin ice shell. *Icarus*, *189*(2), 424–438. https://doi.org/10.1016/j.icarus.2007.02.002

Heimpel, M., & Aurnou, J. (2007). Turbulent convection in rapidly rotating spherical shells: A model for equatorial and high latitude jets on Jupiter and Saturn. *Icarus*, *187*(2), 540–557. https://doi.org/10.1016/j.icarus.2006.10.023

Hindman, B. W., Featherstone, N. A., & Julien, K. (2020). Morphological classification of the convective regimes in rotating stars. *The Astrophysical Journal*, *898*(2), 120. https://doi.org/10.3847/1538-4357/ab9ec2

Johnston, H., & Doering, C. R. (2009). Comparison of turbulent thermal convection between conditions of constant temperature and constant flux. *Physical Review Letters*, *102*(6), 064501. https://doi.org/10.1103/physrevlett.102.064501

Jones, H., & Marshall, J. (1993). Convection with rotation in a neutral ocean: A study of open-ocean deep convection. *Journal of Physical Oceanography*, *23*(6), 1009–1039. https://doi.org/10.1175/1520-0485(1993)023<1009:cwrian>2.0.co;2

Julien, K., Knobloch, E., Rubio, A. M., & Vasil, G. M. (2012). Heat transport in low-Rossby-number Rayleigh-Bénard convection. *Physical Review Letters*, *109*(25). https://doi.org/10.1103/physrevlett.109.254503

Kang, W., Mittal, T., Bire, S., Michel, J., & Marshall, J. (2021). How does salinity shape ocean circulation and ice geometry on Enceladus and other icy satellites? *arxiv*.

Kaspi, Y., & Flierl, G. R. (2007). Formation of jets by baroclinic instability on gas planet atmospheres. *Journal of the Atmospheric Sciences*, *64*(9), 3177–3194. https://doi.org/10.1175/jas4009.1

Kaspi, Y., Flierl, G. R., & Showman, A. P. (2009). The deep wind structure of the giant planets: Results from an anelastic general circulation model. *Icarus*, *202*(2), 525–542. https://doi.org/10.1016/j.icarus.2009.03.026

Kaspi, Y., Galanti, E., Hubbard, W. B., Stevenson, D. J., Bolton, S. J., Iess, L., et al. (2018). Jupiter's atmospheric jet streams extend thousands of kilometres deep. *Nature*, *555*(7695), 223–226. https://doi.org/10.1038/nature25793

Kaspi, Y., Galanti, E., Showman, A. P., Stevenson, D. J., Guillot, T., Iess, L., & Bolton, S. J. (2020). Comparison of the deep atmospheric dynamics of Jupiter and Saturn in light of the Juno and Cassini gravity measurements. *Space Science Reviews*, *216*(5). https://doi.org/10.1007/s11214-020-00705-7

King, E. M., Soderlund, K. M., Christensen, U. R., Wicht, J., & Aurnou, J. M. (2010). Convective heat transfer in planetary dynamo models. *Geochemistry, Geophysics, Geosystems*, *11*(6). https://doi.org/10.1029/2010gc003053

Kunnen, R. P. J. (2021). The geostrophic regime of rapidly rotating turbulent convection. *Journal of Turbulence*, *22*(4–5), 267–296. https://doi.org/10.1080/14685248.2021.1876877

Le, H., & Moin, P. (1991). An improvement of fractional step methods for the incompressible Navier-Stokes equations. *Journal of Computational Physics*, *92*(2), 369–379. https://doi.org/10.1016/0021-9991(91)90215-7

Lobo, A. H., Thompson, A. F., Vance, S. D., & Tharimena, S. (2021). A pole-to-equator ocean overturning circulation on Enceladus. *Nature Geoscience*, *14*(4), 185–189. https://doi.org/10.1038/s41561-021-00706-3

Maas, C., & Hansen, U. (2019). Dynamics of a terrestrial magma ocean under planetary rotation: A study in spherical geometry. *Earth and Planetary Science Letters*, *513*, 81–94. https://doi.org/10.1016/j.epsl.2019.02.016

Manneville, J.-B., & Olson, P. (1996). Banded convection in rotating fluid spheres and the circulation of the Jovian atmosphere. *Icarus*, *122*(2), 242–250. https://doi.org/10.1006/icar.1996.0123

Marshall, J., & Schott, F. (1999). Open-ocean convection: Observations, theory, and models. *Reviews of Geophysics*, *37*(1), 1–64. https://doi.org/10.1029/98rg02739

Matsuyama, I., Beuthe, M., Hay, H. C., Nimmo, F., & Kamata, S. (2018). Ocean tidal heating in icy satellites with solid shells. *Icarus*, *312*, 208–230. https://doi.org/10.1016/j.icarus.2018.04.013

Maxworthy, T., & Narimousa, S. (1994). Unsteady, turbulent convection into a homogeneous, rotating fluid, with oceanographic applications. *Journal of Physical Oceanography*, *24*(5), 865–887. https://doi.org/10.1175/1520-0485(1994)024<0865:utciah>2.0.co;2

Miquel, B., Xie, J.-H., Featherstone, N., Julien, K., & Knobloch, E. (2018). Equatorially trapped convection in a rapidly rotating shallow shell. *Physical Review Fluids*, *3*(5), 053801. https://doi.org/10.1103/physrevfluids.3.053801

Pedlosky, J. (1987). *Geophysical fluid dynamics* (2nd ed.). Springer-Verlag.

Postberg, F., Kempf, S., Schmidt, J., Brilliantov, N., Beinsen, A., Abel, B., et al. (2009). Sodium salts in E-ring ice grains from an ocean below the surface of Enceladus. *Nature*, *459*(7250), 1098–1101. https://doi.org/10.1038/nature08046

Postberg, F., Khawaja, N., Abel, B., Choblet, G., Glein, C. R., Gudipati, M. S., et al. (2018). Macromolecular organic compounds from the depths of Enceladus. *Nature*, *558*(7711), 564–568. https://doi.org/10.1038/s41586-018-0246-4

Ramadhan, A., Wagner, G. L., Constantinou, N. C., Poulin, F. J., Chor, T., Bire, S., et al. (2021). *Clima/Oceananigans.jl: v0.55.1 (Version v0.55.1)*. Zenodo. https://doi.org/10.5281/zenodo.4708225

Ramadhan, A., Wagner, G. L., Hill, C., Campin, J.-M., Churavy, V., Besard, T., et al. (2020). Oceananigans.jl: Fast and friendly geophysical fluid dynamics on GPUs. *Journal of Open Source Software*, *5*(53), 2018. https://doi.org/10.21105/joss.02018

Rekier, J., Trinh, A., Triana, S. A., & Dehant, V. (2019). Internal energy dissipation in Enceladus's subsurface ocean from tides and libration and the role of inertial waves. *Journal of Geophysical Research*, *124*(8), 2198–2212. https://doi.org/10.1029/2019je005988

Rhines, P. B. (1975). Waves and turbulence on a beta-plane. *Journal of Fluid Mechanics*, *69*(3), 417–443. https://doi.org/10.1017/s0022112075001504

Roberts, P. H. (1968). On the thermal instability of a rotating-fluid sphere containing heat sources. *Philosophical Transactions of the Royal Society of London. Series A, Mathematical and Physical Sciences*, *263*(1136), 93–117. https://doi.org/10.1098/rsta.1968.0007

Schumann, U., & Sweet, R. A. (1988). Fast Fourier transforms for direct solution of Poisson's equation with staggered boundary conditions. *Journal of Computational Physics*, *75*(1), 123–137. https://doi.org/10.1016/0021-9991(88)90102-7

Shu, C.-W. (2009). High order weighted essentially nonoscillatory schemes for convection dominated problems. *SIAM Review*, *51*(1), 82–126. https://doi.org/10.1137/070679065

Soderlund, K. M. (2019). Ocean dynamics of outer solar system satellites. *Geophysical Research Letters*, *46*(15), 8700–8710. https://doi.org/10.1029/2018gl081880

Soderlund, K. M., Schmidt, B. E., Wicht, J., & Blankenship, D. D. (2013). Ocean-driven heating of Europa's icy shell at low latitudes. *Nature Geoscience*, *7*(1), 16–19. https://doi.org/10.1038/ngeo2021

Stellmach, S., Lischper, M., Julien, K., Vasil, G., Cheng, J., Ribeiro, A., et al. (2014). Approaching the asymptotic regime of rapidly rotating convection: Boundary layers versus interior dynamics. *Physical Review Letters*, *113*(25), 254501. https://doi.org/10.1103/physrevlett.113.254501

Stoker, C., Boston, P., Mancinelli, R., Segal, W., Khare, B., & Sagan, C. (1990). Microbial metabolism of tholin. *Icarus*, *85*(1), 241–256. https://doi.org/10.1016/0019-1035(90)90114-o

Takehiro, S.-I. (2008). Physical interpretation of spiralling-columnar convection in a rapidly rotating annulus with radial propagation properties of Rossby waves. *Journal of Fluid Mechanics*, *614*, 67–86. https://doi.org/10.1017/s0022112008003194

Thomas, P., Tajeddine, R., Tiscareno, M., Burns, J., Joseph, J., Loredo, T., et al. (2016). Enceladus's measured physical libration requires a global subsurface ocean. *Icarus*, *264*, 37–47. https://doi.org/10.1016/j.icarus.2015.08.037

Trumbo, S. K., Brown, M. E., & Hand, K. P. (2019). Sodium chloride on the surface of Europa. *Science Advances*, *5*(6). https://doi.org/10.1126/sciadv.aaw7123

Tyler, R. (2014). Comparative estimates of the heat generated by ocean tides on icy satellites in the outer Solar System. *Icarus*, *243*, 358–385. https://doi.org/10.1016/j.icarus.2014.08.037

Vance, S., & Goodman, J. (2009). Oceanography of an ice-covered moon. *Europa*, 459–482. https://doi.org/10.2307/j.ctt1xp3wdw.25

Vasil, G. M., Julien, K., & Featherstone, N. A. (2021). Rotation suppresses giant-scale solar convection. *Proceedings of the National Academy of Sciences*, *118*(31), e2022518118. https://doi.org/10.1073/pnas.2022518118

Waite, J. H., Combi, M. R., Ip, W.-H., Cravens, T. E., McNutt, R. L., Kasprzak, W., et al. (2006). Cassini ion and neutral mass spectrometer: Enceladus plume composition and structure. *Science*, *311*(5766), 1419–1422. https://doi.org/10.1126/science.1121290

Williams, G. P. (1979). Planetary circulations: 2. The Jovian quasi-geostrophic regime. *Journal of the Atmospheric Sciences*, *36*(5), 932–969. https://doi.org/10.1175/1520-0469(1979)036<0932:pctjqg>2.0.co;2

Yano, J.-I., Talagrand, O., & Drossart, P. (2005). Deep two-dimensional turbulence: An idealized model for atmospheric jets of the giant outer planets. *Geophysical & Astrophysical Fluid Dynamics*, *99*(2), 137–150. https://doi.org/10.1080/03091920412331336398